THE DEEP2 GALAXY REDSHIFT SURVEY: CLUSTERING DEPENDENCE ON GALAXY STELLAR MASS AND STAR FORMATION RATE AT $Z \sim 1$

Nick Mostek[1], Alison L. Coil[2], Michael Cooper[3], Marc Davis[4], Jeffrey A. Newman[5], and Benjamin J. Weiner[6]

ABSTRACT

We present DEEP2 galaxy clustering measurements at $z \sim 1$ as a function of stellar mass, star formation rate (SFR), and specific SFR (sSFR). We find a strong positive correlation between stellar mass and clustering amplitude on 1-10 h^{-1} Mpc scales for blue, star-forming galaxies with $9.5 < \log(M_*/M_\odot) < 11$ and no dependence for red, quiescent galaxies with $10.5 < \log(M_*/M_\odot) < 11.5$. Using recently re-calibrated DEEP2 SFRs from restframe B-band magnitude and optical colors, we find that within the blue galaxy population at $z \sim 1$ the clustering amplitude increases strongly with increasing SFR and decreasing sSFR. For red galaxies there is no significant correlation between clustering amplitude and either SFR or sSFR. Blue galaxies with high SFR or low sSFR are as clustered on large scales as red galaxies. We find that the clustering trend observed with SFR can be explained mostly, but not entirely, by the correlation between stellar mass and clustering amplitude for blue galaxies. We also show that galaxies above the star-forming "main sequence" are less clustered than galaxies below the main sequence, at a given stellar mass. These results are not consistent with the high-sSFR population being dominated by major mergers. We also measure the clustering amplitude on small scales (≤ 0.3 h^{-1} Mpc) and find an enhanced clustering signal relative to the best-fit large-scale power law for red galaxies with high stellar mass, blue galaxies with high SFR, and both red and blue galaxies with high sSFR. The increased small-scale clustering for galaxies with high sSFRs is likely linked to triggered star formation in interacting galaxies. These measurements provide strong constraints on galaxy evolution and halo occupation distribution models at $z \sim 1$.

Subject headings: galaxies: evolution — galaxies: active — galaxies: high-redshift

1. INTRODUCTION

The non-uniform spatial distribution of galaxies in the Universe, known as large-scale structure, likely reflects the non-uniform spatial distribution of dark matter. Kaiser (1984) showed that galaxies are biased tracers of the total underlying mass distribution. Measurements of galaxy clustering therefore reflect, in part, the clustering of dark matter at a given cosmic epoch. Further, measurements of galaxy clustering over cosmic time constrain the evolving relationship between dark matter, which is governed by gravity and reflects cosmological parameters, and galaxy properties, which are governed by processes associated with baryonic physics. As such, galaxy clustering measurements have the ability to constrain both cosmology (Peacock et al. 2001; Seljak & Warren 2004; Eisenstein et al. 2005) and galaxy evolution physics (Zheng et al. 2007; Conroy & Wechsler 2009; Zehavi et al. 2012) and are thus a powerful tool in the study of large-scale structure formation.

The standard method used to measure galaxy cluster-

njmostek@lbl.gov
[1] Space Sciences Laboratory, University of California, Berkeley, CA, 94720
[2] Center for Astrophysics and Space Sciences, University of California, San Diego, La Jolla, CA, 92093
[3] Center for Galaxy Evolution, Department of Physics and Astronomy, University of California, Irvine, CA, 92697
[4] Department of Astronomy, University of California at Berkeley, Berkeley, CA, 94720
[5] Department of Physics and Astronomy and PITT-PACC, University of Pittsburgh, Pittsburgh, PA, 15620
[6] Steward Observatory, Department of Astronomy, University of Arizona, Tucson, AZ, 85721

ing is the two-point correlation function (2PCF), which quantifies the excess probability of finding a galaxy in a given volume relative to a random distribution (Davis & Peebles 1983; Landy & Szalay 1993). Combined with redshift information, the 2PCF produces a statistical representation of the three-dimensional galaxy density distribution as a function of scale. In recent years, the clustering of galaxies with respect to dark matter has been interpreted using the "halo model" framework. The clustering amplitude of both dark matter particles and dark matter halos can be analytically fit, for a given cosmology, using N-body simulations (Mo & White 1996; Sheth et al. 2001). Simple proposed analytic models describe how galaxies populate dark matter halos as a function of scale and mass (Jing 1998; Peacock & Smith 2000; Seljak 2000; Benson et al. 2000; Cooray & Sheth 2002). In these halo occupation distribution (HOD) models, galaxies populate dark matter halos using a probability distribution generated to match measured galaxy clustering statistics, therefore statistically connecting the baryonic matter of galaxies to the dark matter halos (Berlind & Weinberg 2002). Such HOD models typically include descriptions of the halo structure in terms of the "central" galaxy within a given dark matter halo and the sub-halo "satellite" galaxies that reside within the parent dark matter halo (Kravtsov et al. 2004).

Modern day redshift surveys are uniquely suited to characterize the large-scale galaxy distribution through the 2PCF over a wide range of cosmic time, including surveys of local ($z<0.15$, York et al. 2000; Colless et al. 2001; Abazajian et al. 2009), intermediate ($z \sim 0.5$, Blake et

al. 2009; Eisenstein et al. 2011; Coil et al. 2011), and higher redshift galaxies ($0.7<z<2$, Lilly et al. 2007; van Dokkum et al. 2009; Newman et al. 2012). Such surveys have shown that the clustering of galaxies is correlated with various galaxy properties such as luminosity and color, where the clustering amplitude increases for galaxies with redder color and/or higher luminosity at least to $z<1$ (Coil et al. 2008, hereafter C08; Zehavi et al. 2011).

While there is a strong, demonstrable relationship between galaxy luminosity and color with clustering amplitude, interpreting this relationship in terms of the underlying physics can be complicated, as there are competing effects due to varying star formation histories, mass-to-light ratios, metallicity, dust, and other complex galaxy physics. A cleaner physical relationship in the mapping between galaxies and dark matter halos may be derived from measuring clustering as a function of properties that are easier to interpret, such as stellar mass and star formation rate (SFR). Using these galaxy properties, one may obtain direct constraints on the baryonic processes involved in galaxy evolution rather than with intermediate dependencies on luminosity and color. For example, Zheng et al. (2007) constrained the HOD of the luminosity-dependent clustering results from the SDSS and DEEP2 surveys, but the interpretation is complicated by uncertainties in connecting luminosity and stellar mass for different galaxy populations. Zheng et al. showed that while one can use the HOD to constrain the evolution of the stellar-halo mass relationship, further model refinement requires clustering measurements for galaxy samples selected by stellar mass.

Measuring clustering with respect to galaxy properties has been made possible by the advent of large redshift surveys in the last decade. Using the SDSS, Li et al. (2006) found that on large scales (> 1 h^{-1} Mpc), the dependence of galaxy clustering on stellar mass closely mirrors that of luminosity; the clustering bias is relatively flat below the characteristic stellar mass scale M^* and increases exponentially above M^*. They further investigate how the clustering amplitude depends on other galaxy color, morphology, and stellar mass, and find significant scale-dependent differences at low stellar mass ($\log(M_*/M_\odot)\lesssim10$) between red and blue galaxy samples. At higher redshift ($z\sim0.85$), Meneux et al. (2008) measured the clustering of ≈3200 galaxies in the VVDS (Le Fevre et al. 2003) selected by stellar mass. Similar to the local behavior, Meneux et al. found that the clustering amplitude increases with stellar mass and that the clustering amplitude at $9.5<\log(M_*/M_\odot)<10.5$ is systematically lower than in local samples. The clustering amplitude at higher stellar masses ($\log(M_*/M_\odot)>10.5$) has not evolved in the same span of time within the measurement errors.

While it is preferable to measure the 2PCF using spectroscopic redshifts, several studies have used photometric redshifts to measure the two-dimensional angular correlation function with respect to stellar mass. Because photometric redshifts depend only on accurate panchromatic photometry, larger sample sizes are more easily obtained, particularly at higher redshifts where spectroscopy requires extensive telescope resources. Using data from the NEWFIRM Medium Band Survey (NMBS, van Dokkum et al. 2009) between $1<z<2$, Wake et al. (2011) used angular clustering measurements to find that a positive

correlation exists between stellar mass and halo mass to $z<2$. Leauthaud et al. (2012) also used the angular correlation function along with weak lensing maps from COSMOS (Capak et al. 2007; Ilbert et al. 2009) to fit an HOD model between $0.2<z<1$. They find that the peak of the ratio of $M_*/M_{\rm halo}$ is a constant with cosmic time, indicating a fundamental connection between the fraction of baryons within a given halo mass and the conversion rate of those baryons into stars. While angular clustering though photo-zs is less precise than the 2PCF, some of the most advanced HOD models to date have been built off such data.

In contrast to stellar mass, there has been very little study of how galaxy clustering depends on SFR. For local galaxies, Li et al. (2008) used SFRs of SDSS galaxies to study the clustering dependence on the specific star-formation rate (sSFR, the SFR divided by stellar mass), though not the dependence on SFR alone. At higher redshifts ($z\sim2$), a recent study by Lin et al. (2012) measured the angular correlation function for BzK-selected star-forming galaxies in 160 arcmin^2 of the GOODS-North field (Giavalisco et al. 2004). Lin et al. found a significant large-scale clustering dependence with increasing SFR and decreasing sSFR. However, no clustering analyses using SFR or sSFR have been performed at $z\sim1$ where the global SFR is rapidly declining (Hopkins & Beacom 2006; Zhu, Moustakas & Blanton 2009).

The effects of galaxy clustering on SFR are interesting for HOD models as the parent dark matter halos of galaxies may influence the SFR through various mechanisms. For galaxy populations that are highly clustered and therefore reside in massive halos, the available gas in the galaxy may have been stripped, depleting the galaxy of the material necessary to sustain further star formation. Alternatively, the gas may be heated to the virial temperature of the host halo, such that the cooling time becomes long enough to suppress star formation. However, such star formation "quenching" could arise from secular evolution, which would not necessarily be dependent upon host halo properties. Similarly, the sSFR is a measure of the SFR relative to the existing stellar mass in a galaxy and reflects how *efficiently* a galaxy is processing gas into stars. Determining the clustering properties and galaxy bias with respect to SFR and sSFR as a function of redshift is therefore crucial to understanding how the host dark matter halo and surrounding environment of a galaxy play a role in the evolution of star formation.

While clustering analyses of the 2PCF as a function of stellar mass and SFR are relatively rare at intermediate redshifts, there are measurements of the relationship between these parameters and galaxy environment. Environment studies generally measure the galaxy overdensity for a given population relative to the mean density at the same redshift, often using the Nth nearest neighbor statistic (see Muldrew et al. (2012) for a review of various environmental measures). The advantage of using the local environment is that it provides better statistics in what is essentially a cross-correlation between a given galaxy sample and the mean density field, rather than the auto-correlation that is used in 2PCF analyses. However, environmental analyses can be difficult to model and compare to mock galaxy simulations, in part because the mean observed galaxy density is subject to selection effects that depend on the particular

survey. More importantly, density measurements often average across a range of physical scales (typically with a mean scale of $\gtrsim 1h^{-1}$ Mpc at $z\sim 1$) to infer correlations. Because the "density-defining" population is generally measured on scales that are roughly the size of a halo, such measurements preclude smaller sub-halo scales. For example, Li et al. (2006) measured the 2PCF of SDSS galaxies with respect to their structural parameters and found significant clustering dependence on scales below <1 h^{-1} Mpc, a result that was not previously seen in environment studies. The scale-dependence of clustering as a function of galaxy properties can yield important clues as to the physical processes involved in galaxy formation and evolution.

As environment and 2PCF analyses are complementary, it is important to compare the trends found in both kinds of studies to test for consistency, particularly on large scales. Cooper et al. (2008, hereafter CP08) used data from SDSS and DEEP2 to quantify the evolution of the relationships between SFR and sSFR with environment. They found that the relation between sSFR and overdensity is essentially unchanged with redshift, suggesting that mergers did not drive the decline in the global SFR at $z<1$. Confirming the results from Elbaz et al. (2007), CP08 also found that galaxies with high SFRs are found in high density environments at $z\sim 1$, which leads to an "inversion" of the SFR-density relationship between $z\sim 1$ and $z\sim 0$, where high-SFR galaxies are found in relatively sparse environments.

Other studies have measured the evolution of galaxy environment with respect to SFR at a fixed stellar mass between $0.2<z<1$. Several studies report that the average color-density relation does not appear to have evolved since $z<1$, indicating that the sSFR-density relationship is relatively constant with cosmic time since $z=1$ (Cucciati et al. 2006; Scodeggio et al. 2009; Peng et al. 2010; Sobral et al. 2010; Grützbauch et al. 2011). These findings generally agree with the studies within CP08, with the caveat that finer sub-sampling of the most extreme density regions can reveal a statistically significant difference in galaxy restframe colors (Cooper et al. 2010). Similarly, Scodeggio et al. (2009) and Peng et al. (2010) find that bulk trends in the SFR-density relation for field galaxies (typically with $\log(M_*/M_\odot)<11$) can also be explained by the change in stellar mass at a fixed SFR. Sobral et al. (2010) goes on to suggest that most, but not all, of the SFR-density correlation is due to changes in stellar mass in highly star-forming galaxies. The general consensus from these studies is that there is a fundamental relationship between stellar mass and large-scale environment and that correlations between environment and other galaxy properties are due to second-order effects.

In this paper, we quantify the relationship between dark matter halos and galaxy properties at $z\sim 1$ by measuring the clustering of DEEP2 galaxy samples selected by stellar mass, SFR, and sSFR, on scales of $\sim 0.1-20$ h^{-1} Mpc. Our results will enable future HOD modeling studies at $z\sim 1$ as a function of these galaxy properties and will further be useful for projecting the statistical power expected from large-area baryon acoustic oscillation (BAO) surveys at these redshifts (e.g. Big-BOSS, Schlegel et al. 2011; Mostek et al. 2012b). The

structure of the paper is as follows. In Section 2, we present the DEEP2 dataset and derived galaxy properties used in this study. In Section 3, we describe the galaxy samples defined by stellar mass, SFR, and sSFR. Section 4 details the clustering analysis methods using the 2PCF, while Section 5 presents the results of our clustering analysis with respect to the various galaxy properties. We compare our findings to the recent literature and discuss the broader implications of our results in Section 6, and we present our conclusions in Section 7. Throughout this work, we assume a ΛCDM cosmology with Ω_M=0.3, Ω_Λ=0.7, σ_8=0.8, and $h=0.7$. All quoted magnitudes are in the AB magnitude system.

2. DATA

The DEEP2 Galaxy Redshift Survey (Newman et al. 2012) is one of the largest, most complete spectroscopic redshift surveys of the Universe to $z\sim 1$. The DEEP2 survey was conducted on the Keck II telescope using the DEIMOS spectrograph (Faber et al. 2003) and measured reliable redshifts for 31,656 galaxies from $0<z<1.4$ over four fields dispersed across the Northern Sky. The DEEP2 survey targeted galaxies to a magnitude limit of $R_{AB} <24.1$, and in three of the four fields used a BRI color cut to efficiently target galaxies with $z>0.7$.

For this study, we initially select galaxies with $0.74<z<1.4$ and a high confidence redshift ($>95\%$, $z$quality ≥ 3). As we are interested in measuring clustering properties as a function of galaxy properties, we retain only those galaxies with well-measured values of restframe B-band magnitude (M_B), color ($U-B$), stellar mass (M_*), and star-formation rate (SFR or ψ). Because the average SFRs are now estimated from the galaxy luminosity and restframe color (Mostek et al. 2012a), we do not exclude red galaxies in our sample. These combined selections result in a parent sample of 22,331 galaxies.

2.1. Calibrations of Stellar Mass and SFR

The stellar masses used in this study are constructed from the prescription described in Lin et al. (2007) and the Appendix of Weiner et al. (2009), where the local restframe color-M/L relation (Bell et al. 2003) is extended to higher redshift. The prescription depends on redshift, restframe B-band luminosity, and the restframe $U-B$ and $B-V$ colors, and is calibrated to a matched sample of stellar masses derived from K-band luminosity measurements (Bundy et al. 2006). Figure 1 compares stellar masses from the DEEP2 calibration with those from a matched sample of 7,267 K-band stellar masses (K. Bundy, priv. communication) for galaxies with $0.74<z<1.4$. We confirm that the stellar masses used here are in agreement with K-band derived masses with a rms scatter of 0.25 dex and a mean offset of -0.05 dex. The DEEP2 stellar masses are based on a Chabrier IMF, in keeping with the Weiner et al. calibration.

In CP08, SFRs for DEEP2 galaxies were derived from measurements of the [O II] emission line and an empirical calibration to galaxy B-band luminosity and SFR performed at low redshift (Moustakas, Kennicut & Tremonti 2006). Applying this local calibration to redshifts $z\sim 1$ poses some unique problems, including accounting for luminosity and dust evolution as well as line emission from AGN in red sequence galaxies (Yan et al., 2006).
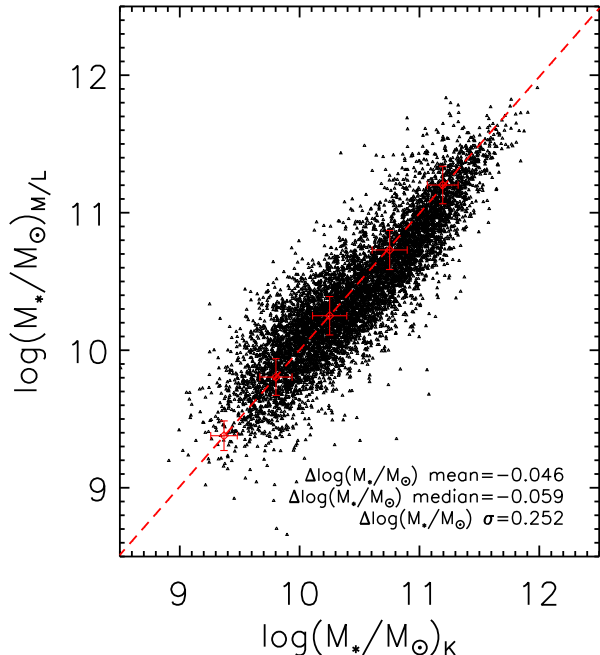
FIG. 1.— Comparison of DEEP2 color-M/L stellar masses and K-band stellar masses. The rms scatter between the stellar mass estimates is 0.25 dex and the sample mean offset is -0.05 dex for a Chabrier IMF.

More recent work by Mostek et al. (2012a) established a new empirical SFR calibration for DEEP2 galaxies using broadband optical color and UV/optical SED-based SFRs (Salim et al. 2009). Mostek et al. showed that the strong observed evolution in the restframe M_B from local redshifts (~ 1.3 mag to $z = 1$) caused the SFRs in CP08 to be overestimated by an average of ~ 0.5 dex. However, as this evolution causes to first order a zero-point offset in the SFR calibration, the relative trends between SFR and overdensity presented in CP08 are still valid. Here we use the Mostek et al. SFR calibration and a Salpeter IMF, in keeping with previous SFR calibrations commonly used in the literature (Kennicutt 1998; Moustakas, Kennicut & Tremonti 2006).

The sSFRs used here are constructed from the DEEP2 stellar masses and SFRs described above, using $\log(\psi/M_*) \equiv \log(M_*/M_\odot) - \log(\psi)$. We convert the stellar masses from a Chabrier IMF to a Salpeter IMF by adding a constant 0.2 dex offset and quote sSFRs for a Salpeter IMF. We note that both the (Moustakas, Kennicut & Tremonti 2006) and Mostek et al. (2012a) SFR calibrations rely on correlated mean trends in large galaxy samples, and therefore may not be highly accurate on a individual galaxy-by-galaxy basis (typically 0.2-0.3 dex rms scatter). However, the *samples* selected from such empirical SFR calibrations are statistically representative of the mean SFR in the galaxy population.

As clustering measurements are more commonly performed as a function of galaxy luminosity and color, we show in Figure 2 how our derived stellar masses, SFRs, and sSFRs depend on restframe color and magnitude, showing contours of each derived property in the $U - B$ - M_B plane. The contours of constant stellar mass generally run perpendicular to the contours of constant SFR in this plane. When converted to sSFR,

these opposing trends cancel out to produce a largely luminosity-independent trend with color, reflecting the fact that sSFR and restframe color generally reflect the light-averaged age of the stellar population.

3. GALAXY SAMPLES

In this section, we describe the construction of samples for $0.74<z<1.4$ DEEP2 galaxies selected by stellar mass, SFR, and sSFR. For galaxy clustering measurements, it is preferable to use complete samples for which galaxies of the same 'type' (selected by magnitude, color, stellar mass, etc.) are included to the highest redshift of the sample. In this way, within a given sample there is no redshift dependence of the galaxy property of interest, which would necessitate weighting each galaxy by the volume over which it could be observed. Complete galaxy samples also facilitate comparison with simulations and HOD modeling, where a galaxy population can be well described by a few simple selection criteria and a redshift limit.

We create both binned and threshold samples in this study. Constructing samples with independent bins facilitates identification of clustering trends with respect to each galaxy parameter, while constructing threshold samples facilitates future HOD modeling applications. The binned sample sizes are chosen such that the bin size is greater than or equal to the rms scatter in the galaxy property and so that there is a sufficient number of galaxies per bin to minimize Poisson errors. For each galaxy parameter, we treat the bin with the lowest number density, which generally corresponds to the more massive or higher SFR galaxies, as a threshold lower limit.

Our galaxy samples cover two primary redshift ranges: $0.74<z<1.05$ for samples that are complete for both blue and red galaxies, and $0.74<z<1.4$ for samples that are complete only for blue galaxies. The former redshift range allows us to compare clustering trends between galaxies with different star-formation histories - including both quiescent and star-forming galaxies - while the latter allows us to obtain the best statistical measurements for blue galaxies.

3.1. *Stellar Mass*

As shown in the left panel of Figure 2, galaxy samples selected by stellar mass naturally include both red and blue galaxies, but the ratio of red to blue galaxies strongly depends on stellar mass. In addition, the R-band selection of DEEP2 corresponds to a different rest-frame wavelength selection with redshift (bluer at higher redshift), such that DEEP2 is complete to different stellar masses for red and blue galaxies as a function of redshift. To probe the full range of stellar masses allowed by the data, we construct both color-independent (e.g. 'all' galaxies, blue and red) and color-dependent stellar mass samples for $z<1.05$, and we construct mass samples for blue galaxies only for $z<1.4$. Following Willmer et al. (2006), we use the standard DEEP2 red and blue galaxy separation defined by

$$(U - B) = -0.032(M_B + 21.62) + 1.035. \qquad (1)$$

Using this color separation, the left panel of Figure 3 shows stellar masses for red and blue DEEP2 galaxies as a function of redshift, with boxes indicating our
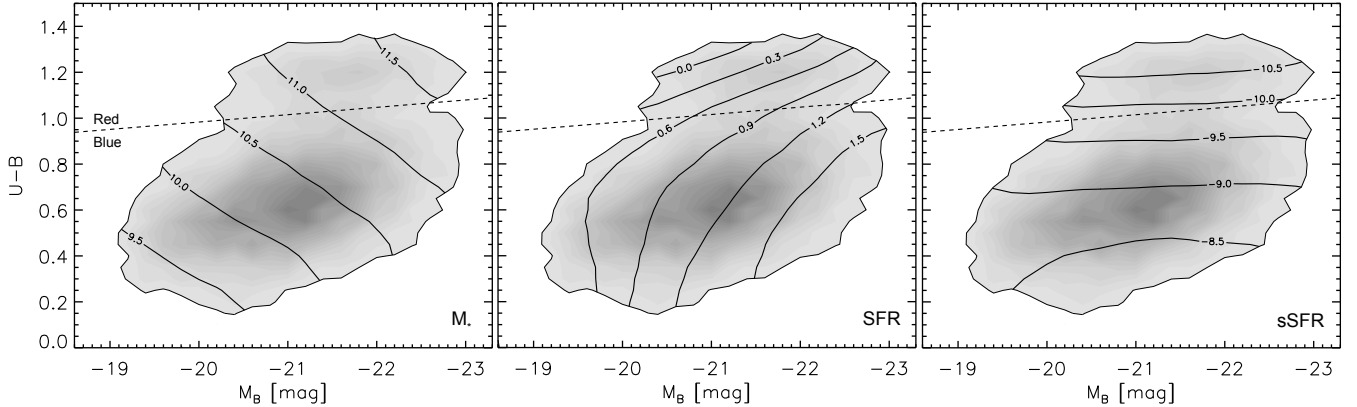
FIG. 2.— The greyscale in all three panels shows the restframe $U-B$ color and B-band magnitude distribution for the $0.74<z<1.4$ DEEP2 galaxy sample. (left) Stellar mass contours span $9.0<\log(M_*/M_\odot)<11.5$ with levels of $\Delta\log(M_*/M_\odot)=0.5$. More massive galaxies tend to be redder and brighter. The dashed line shows the DEEP2 restframe galaxy color selection from Equation 1 splitting the red sequence and blue cloud. (middle) SFR contours calibrated from Mostek et al. (2012a) spanning $0<\log(\psi)<1.5$ and levels of $\Delta\log(\psi)=0.3$ $M_\odot$ yr^{-1}. Galaxies with higher SFR are bluer and brighter. SFRs are correlated in restframe M_B and $U-B$ partially by construction, where optical photometry has been used in the calibration. (right) Contours of sSFR spanning $-8.5>\log(\psi/M_*)>-11$ with levels of $\Delta\log(\psi/M_*)=0.5$ yr^{-1}. Galaxies with higher sSFR are bluer; $U-B$ color and sSFR correlate tightly, as evidenced by the horizontal contours.
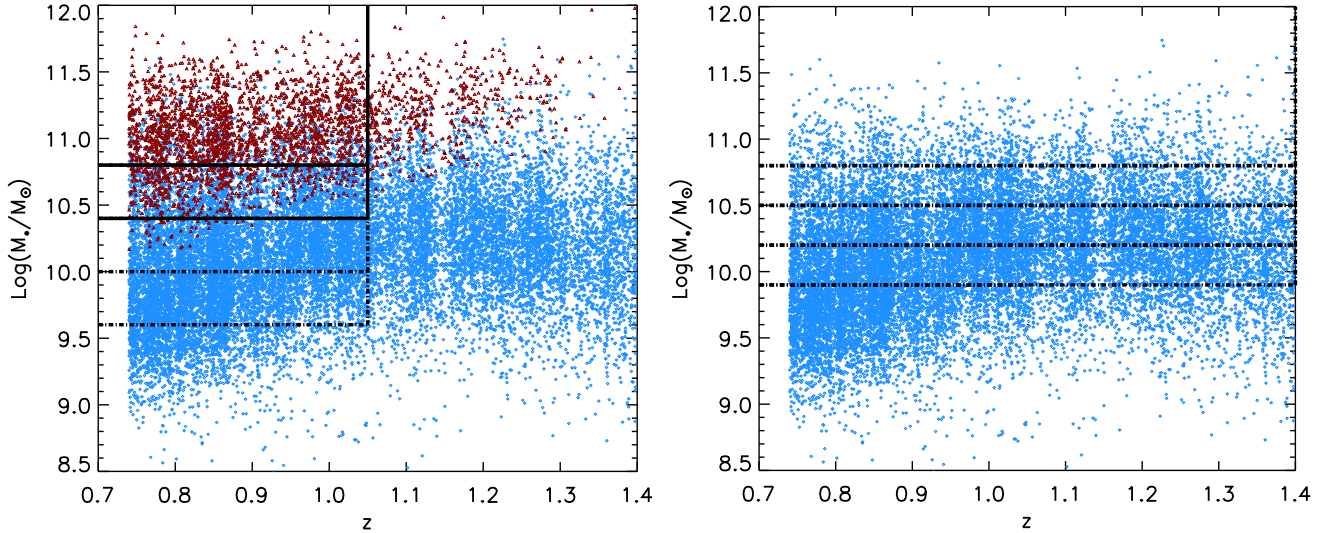

FIG. 3.— Stellar mass selected galaxy samples. (left) Colored points show all galaxies in the parent sample, where red galaxies are defined to be redder than the color cut given in Equation 1. Solid lines show the mass limits for color-independent galaxy samples, where the highest mass sample is roughly volume-limited for both red and blue galaxies. Dot-dashed lines show the lower mass sample limits for blue galaxies only at a $z<1.05$ redshift limit. Red galaxy mass sample limits are given in Tables 1 and 2. (right) Stellar mass bin samples for blue galaxies only, defined with finer $\Delta\log(M_*/M_\odot)=0.3$ bins and approximately complete in DEEP2 to $z<1.4$. The highest mass bin in both samples are implemented as a mass threshold in order to allow sufficient statistics in the clustering measurement.

binned samples to $z=1.05$. As a starting point, we define color-independent samples including both red and blue galaxies in two bins in stellar mass. For the highest stellar mass sample, we use a mass threshold of $\log(M_*/M_\odot)>10.8$ to ensure a large enough sample size such that clustering measurements can be performed with reasonable accuracy. This high-stellar-mass sample is roughly volume-limited for both red and blue galaxies in this stellar mass range. The lower stellar mass color-independent mass bin spans $10.4<\log(M_*/M_\odot)<10.8$ but is somewhat incomplete for red galaxies at $z\sim1$ due to the R-band magnitude limit in DEEP2. In this mass bin, 30% of the galaxies between $0.75<z<0.85$ are red while only 12% of galaxies between $0.95<z<1.05$ are red, indicating that red galaxies are increasingly excluded at the highest redshifts. Therefore, we can construct

only one sample that is complete for both red and blue galaxies (with $\log(M_*/M_\odot)>10.8$), and while we quote results from the lower mass color-independent bin, we refrain from calculating a number density in this sample. We further caution that this sample underestimates the contribution from low mass, high redshift red galaxies missing in DEEP2, and we keep this in mind when interpreting the results.

In order to compare the clustering of red and blue galaxies separately as a function of stellar mass, we also create red and blue mass-selected samples. The mass and redshift limits of each sample are given in Table 2, and the blue samples are shown in Figure 3. For red galaxies, we create two samples with $10.5<\log(M_*/M_\odot)<11.0$ and $\log(M_*/M_\odot)>11.0$ at $z<1.05$. To facilitate comparison with red galaxies over the same volume, we create three

blue mass-limited bin samples down to a lower mass of $\log(M_*/M_\odot)>9.6$, where the blue population is complete at $z = 1.05$. We further create blue mass-limited bin samples over a wider redshift range, to $z = 1.4$, down to a mass of $\log(M_*/M_\odot)=9.9$ (right panel of Figure 3). The blue galaxy mass bin samples to $z=1.4$ have a slightly smaller width (0.3 dex) than the lower redshift samples (0.4 dex), but the width is still greater than the rms scatter in the stellar mass estimates (0.25 dex, see Figure 1). An upper threshold limit of $\log(M_*/M_\odot)>10.8$ is used to define the highest mass bin.

We also define stellar mass-selected *threshold* samples (not shown in Figure 3) with which to measure clustering properties. These threshold samples are useful for comparing with simulations and semi-analytic models, where samples may be defined by a given mass limit, and for performing HOD modeling. For the color-independent stellar mass threshold samples, we only report the number density for stellar masses above $\log(M_*/M_\odot)>10.5$ due to the limited number of red galaxies in the measured volume. The sample properties for each stellar mass-selected sample are listed in Tables 1 and 2.
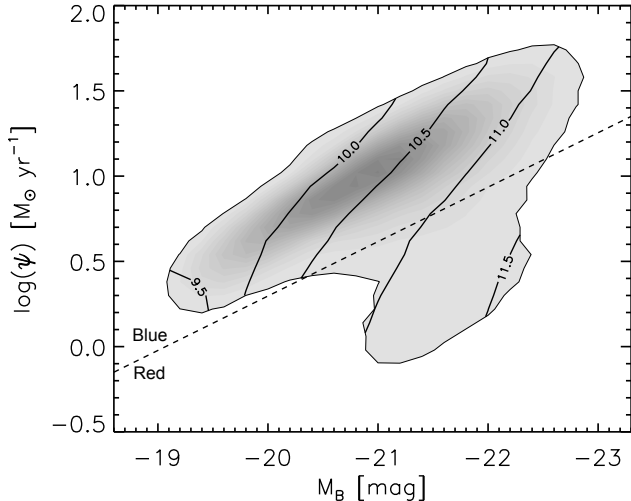

FIG. 4.— SFRs using the Mostek et al. (2012a) calibration versus M_B. Greyscale shows the distribution of DEEP2 galaxies between $0.74<z<1.4$. Contours show lines of constant stellar mass, with the same mass levels as in Figure 2. The dashed line shows the approximate demarcation between red and blue galaxies, as defined in the color-magnitude diagram and Equation 1.

3.2. *Star Formation Rate*

As with stellar mass, galaxies at a given SFR can have a range of restframe color and magnitude. Figure 4 shows the SFRs for DEEP2 galaxies as a function of M_B; the dashed line indicates the separation of red and blue galaxies following Equation 1. While most red galaxies have an estimated SFR below $\log(\psi)<0.5$ $M_\odot$ yr^{-1}, only those blue galaxies with $M_B <-20$ have similar SFRs. Figure 4 also shows that SFR samples will select across a wide range of stellar mass (shown with contours), particularly for blue galaxies where M_* can differ by 1.5 dex at a given SFR. Therefore, our analysis using SFR-selected samples not only probes the relationship between clustering and SFR but also has a weak dependence on stellar mass. We will explicitly remove

the stellar mass dependence by constructing specific SFR samples in Section 3.3.

While one could in theory construct color-independent samples in SFR given a large enough survey, DEEP2 does not have a sufficient number of both red and blue galaxies at a constant SFR and complete within the same volume to obtain a reliable color-independent clustering measurement. We therefore create color-dependent SFR samples that are approximately complete within their restframe color as shown in Figure 5. To mirror the selection with stellar mass, we choose red galaxies with $z<1.05$ in two SFR samples limited to $-0.1<\log(\psi)<0.3$ $M_\odot$ yr^{-1} and $\log(\psi)\geq0.3$ $M_\odot$ yr^{-1}. As SFR is strongly dependent on M_B, particularly in blue galaxies, the redshift completeness limits are clear; blue galaxies are complete for $\log(\psi)>0.75M_\odot$ yr^{-1} below $z<1.05$, $\log(\psi)>1.0M_\odot$ yr^{-1} for $z<1.25$, and $\log(\psi)>1.25M_\odot$ yr^{-1} for $z<1.4$. The SFR bin sizes are selected to roughly reflect the SFR accuracy quoted in Mostek et al. (0.5 dex and 0.25 dex rms scatter for red and blue galaxies, respectively), while maintaining sufficient sample sizes in each bin. The sample properties for each SFR sample are listed in Tables 3 and 4.

3.3. *Specific Star Formation Rate*

To construct highly-complete samples selected by sSFR, we first emphasize that sSFR, as shown in Figure 2, is tightly correlated with restframe color. Similarly, we find that plotting the sSFR against the restframe B-band magnitude (Figure 6) shows that nearly all DEEP2 blue galaxies with $0.74<z<1.4$ have sSFRs between $-10<\log(\psi/M_*)>-8$ yr^{-1}, while red galaxies have lower sSFRs of $\log(\psi/M_*)<-10$ yr^{-1}. Figure 6 also shows that like SFR, galaxies at a fixed sSFR have a wider range of stellar masses (represented by contour lines) in the blue galaxy population than red galaxy population. Further, a sSFR-selected blue galaxy sample will have a residual correlation between the the mean stellar mass and luminosity of the sample. This residual correlation indicates that galaxy luminosity is only a rough approximation to the stellar mass within the blue population at $z \sim 1$.

Stellar mass and SFR each have different completeness limits in DEEP2 as a function of redshift, color, and magnitude, which could in principle be difficult to disentangle when combined as sSFR. However, we can avoid these complications by recognizing that sSFR closely traces color. We can therefore first limit the parent sample by restframe B-band magnitude, M_B, for red and blue galaxies separately, and then define sSFR-selected subsamples free from incompleteness expected at lower luminosities within each restframe color. The final color-dependent sSFR samples will then be complete *to the magnitude limit of the sample*.

The upper panels of Figure 7 show M_B as a function of redshift for red and blue galaxies separately. At $z<1.05$, the parent sample is complete for $M_B<-21$ and $M_B<-20.5$ for red and blue galaxies, respectively. At $z<1.4$ the blue galaxy sample is limited to $M_B<-21$. We choose not to use a more complicated, color-dependent magnitude limit (see Gerke et al. 2007) so that our samples can be easily interpreted in comparison to other sSFR clustering studies.
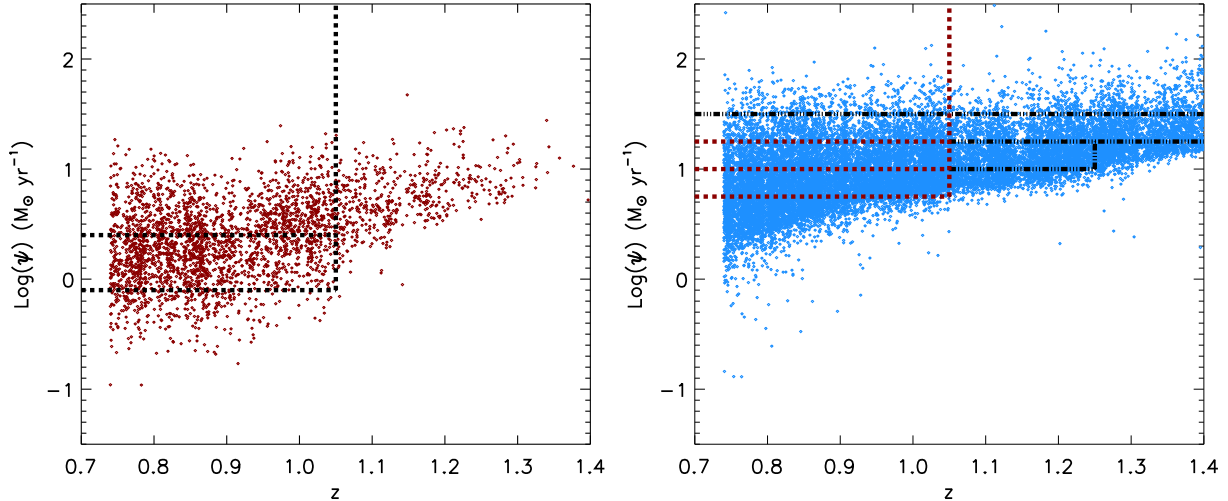
FIG. 5.— Galaxy samples defined by star formation rate. (left) SFR versus redshift for all red galaxies in the parent sample. SFR-selected bin samples for red galaxies are shown with dashed lines; these samples are complete at $z=1.05$ for $\log(\psi)>0.3$ and approximately complete for $\log(\psi)>-0.1$. (right) SFR versus redshift for all blue galaxies in the parent sample. SFR-selected bin samples for blue galaxies complete to $z=1.05$ are shown with red, dashed lines, while samples complete to either $z=1.25$ or $z=1.4$ are shown with black, dot-dashed lines. As with stellar mass, the highest SFR samples are treated as thresholds.
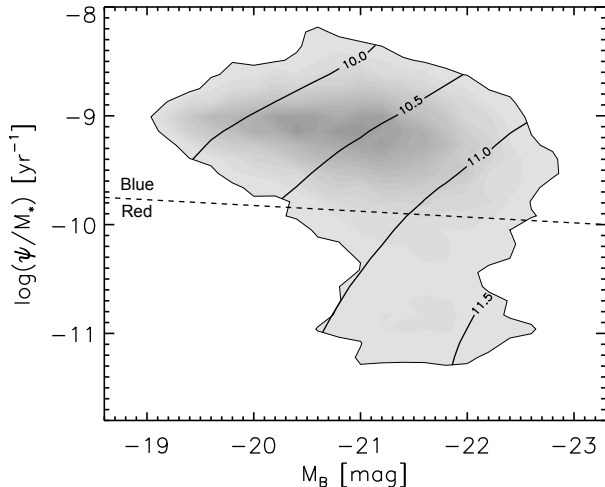

FIG. 6.— Galaxy specific SFR versus the restframe B-band magnitude, M_B. Contours correspond to constant stellar mass, with the same levels shown as in Figure 2.

After making these initial cuts on M_B and redshift, we can construct sSFR samples that are complete to the given M_B limit. The bottom row of Figure 7 shows our sSFR-selected samples. In general, the lowest luminosity galaxies have the highest sSFRs. We define upper limits on sSFR of $\log(\psi/M_*)<-9.9$ $M_\odot$ yr^{-1} for red galaxies and $\log(\psi/M_*)<-8.6$ $M_\odot$ yr^{-1} for blue galaxies. We also limit the blue galaxy population at $z<1.05$ and $z<1.4$ in order to facilitate comparisons with the stellar mass and SFR-selected samples. The individual sSFR sample properties are given in Tables 5 and 6.

4. ANALYSIS METHOD

4.1. *The two-point correlation function*

The clustering analysis performed in this study mirrors that of C08, and we summarize the methodology here. We measure the clustering of DEEP2 galaxies by calculating the two-point correlation function, $\xi(r)$, in each of the galaxy samples. In a given volume, $\xi(r)$ measures the excess probability of finding galaxy pairs as a function of separation over that of a random distribution. The excess probability can be calculated using the Landy & Szalay (1993) estimator,

$$\xi = \frac{1}{RR}\left[DD\left(\frac{n_R}{n_D}\right)^2 - 2DR\left(\frac{n_R}{n_D}\right) + RR\right]. \quad (2)$$

Here RR, DD, and DR are the random-random, data-data, and data-random pairs, while n_R and n_D are the mean number densities of random points and galaxies in each sample. Each pair is separated by a three-dimensional distance r. As such, $\xi(r)$ reflects the three-dimensional clustering, which must be inferred through measurements of the angular separation between galaxies on the sky and a distance measurement along the line of sight.

The redshift of a galaxy reflects both its distance (assuming a given cosmology) and its peculiar velocity. Due to the latter effect, the observed clustering signal has additional power that appears in redshift space but is not attributable to clustering in real space. On small scales, the peculiar velocities of individual galaxies within collapsed overdensities results in an "elongation" of the clustering signal along the line of sight, known as the "Fingers of God". On larger scales, the coherent infall of galaxies streaming into potential wells causes a "squashing" of the signal along the line of sight. To remove these redshift-space distortions from the real-space clustering signal, we separate the correlation function using two separate coordinate vectors. We define two vectors, $\boldsymbol{s}=(\boldsymbol{v}_1-\boldsymbol{v}_2)$ for the redshift-space separation and $\boldsymbol{l}=\frac{1}{2}(\boldsymbol{v}_1+\boldsymbol{v}_2)$ for the mean coordinate of the pair, and calculate

$$\pi = \frac{\boldsymbol{s}\cdot\boldsymbol{l}}{|\boldsymbol{l}|}, \quad (3)$$

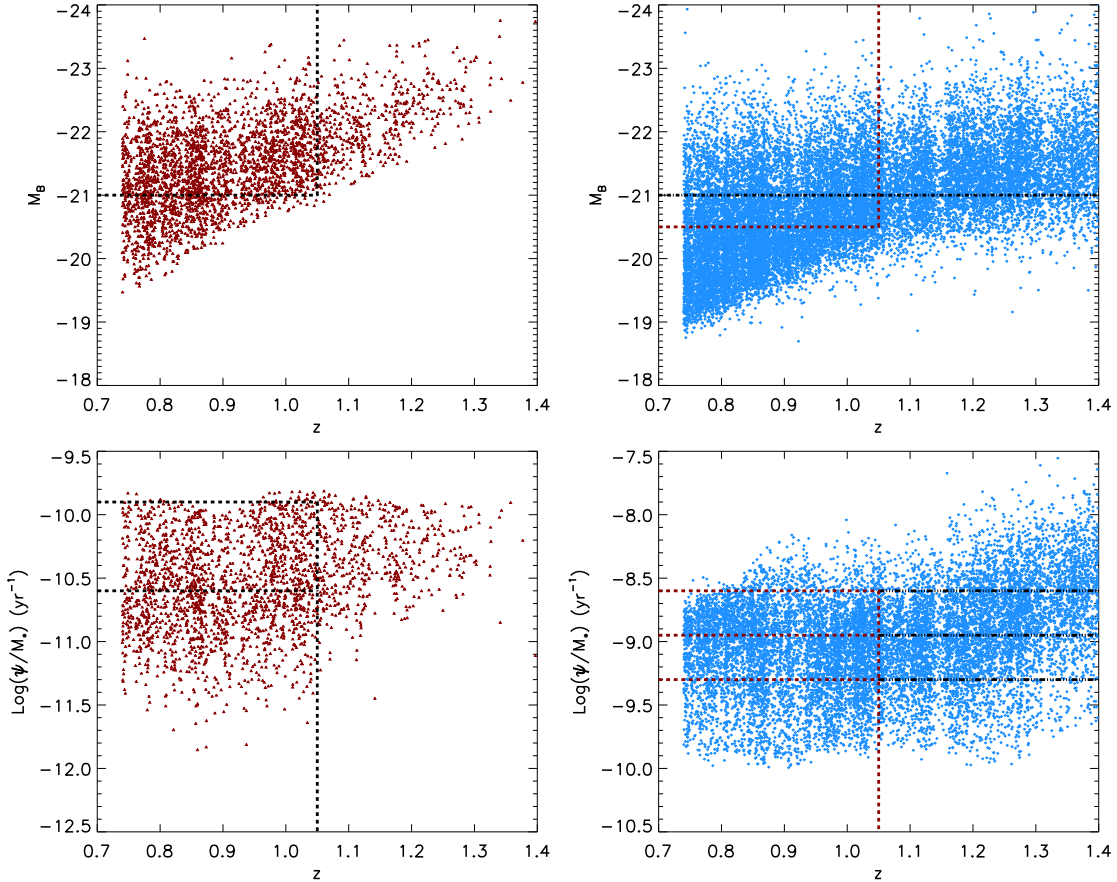$$r_p = \sqrt{\boldsymbol{s}\cdot\boldsymbol{s} - \pi^2}. \quad (4)$$

Fig. 7.— Galaxy samples defined by specific star formation rate. (Top row) Restframe B-band magnitude for red (left) and blue (right) galaxies in the parent sample are shown as a function of redshift. To $z=1.05$, the red galaxies are complete to $M_B=-21$ while blue galaxies are complete to $M_B=-20.5$. To $z=1.4$, blue galaxies are limited to $M_B=-21.0$. (Bottom row) From the magnitude-limited samples defined in the top row, we create sSFR-selected samples with $\log(\psi/M_*)<-9.9$ for red galaxies and $\log(\psi/M_*)<-8.6$ for blue galaxies.

We then can express the three-dimensional $\xi(r)$ as a two-dimensional projection, $\xi(r_p, \pi)$, where r_p is the distance across the line of sight and π is the distance along the line of sight. We apply the estimator in Equation 2 to $\xi(r_p, \pi)$ by counting galaxy pairs. The random samples are drawn from the measured selection function for each galaxy sample spatial distribution (see Section 4.2).

In order to recover the correlation function signal without redshift space distortions, we project the two-dimensional correlation function $\xi(r_p, \pi)$ onto the r_p co-ordinate across the line of sight. The projection requires integrating along the line of sight, following Davis & Peebles (1983),

$$\omega_p(r_p) = 2 \int_0^\infty d\pi \, \xi(r_p, \pi) = 2 \int_0^\infty dy \, \xi \left(r_p^2 + y^2\right)^{1/2}, \quad (5)$$

where y is the real-space separation along the line of sight. By modeling $\xi(r)$ as a power law, $\xi=(r/r_0)^{-\gamma}$, Equation 5 has an analytical solution,

$$\omega_p(r_p) = r_p \left(\frac{r_0}{r_p}\right)^\gamma \frac{\Gamma(1/2)\Gamma[(\gamma-1)/2]}{\Gamma(\gamma/2)}, \quad (6)$$

which can be evaluated for given values of the clustering length, r_0, and correlation function slope, γ. Following C08, we integrate the projected correlation function $\omega_p(r_p)$ to a limit of $\pi_{\max} = 20 \, h^{-1}$ Mpc, beyond which

the DEEP2 sample is not large enough to measure an accurate signal. Implementing the $\pi_{\max}$ limit requires that we also correct Equation 6 to be truncated to the same integration limit. However, the resulting $\omega_p(r_p)$ is accurate for measured scales where $r_p/\pi_{\max} \lesssim 0.25$ (see C08 for details).

We fit for a power law of the form $\xi=(r/r_0)^{-\gamma}$ on scales of 1-10 h^{-1} Mpc. As we will show, these scales mitigate the effects of non-linear behavior at smaller r_p and avoid noisy data at larger scales. The final values of r_0 and γ are obtained by performing a χ^2 minimization between the measured $\omega_p(r_p)$ and Equation 6, after correcting for the truncation of $\pi_{\max}$.

For each sampled scale, galaxy pair counts are averaged over 10 separate DEEP2 pointings and errors on $\omega_p(r_p)$ are computed using the standard error among these pointings. While formal errors for r_0 and γ are computed from the χ^2 fit, we report the rms errors for each parameter using 10 jackknife samples of the data. The jackknife error estimates on r_0 and γ encapsulate the cosmic variance inherent within the DEEP2 data and take into account the covariance among the r_p bins. Because some DEEP2 pointings are correlated with each other on the sky, the cosmic variance may be slightly underestimated. Based on calculations with QUICKCV (Newman & Davis 2002), the actual rms error due to cosmic variance could be up to $\sim 6\%$ larger than the es-

timates from the 10 jackknife samples. We do not include this estimated error contribution in our analysis, electing instead to work with the error given directly from the data.

In order to facilitate interpretation of the results and to avoid relying solely on power-law fits which may not describe the data well over all scales, we further estimate the galaxy bias for each sample. The bias is a measure of the clustering of galaxies relative to that of dark matter at the same redshift. We generate a dark matter $\xi(r_p,\pi)$ for the mean redshift of each galaxy sample using code from Smith et al. (2003), integrating to the same π_{max} as in the data. We then calculate the average bias over scales of 1-10 h^{-1} Mpc using $b^2 = [\omega_p(r_p)]_{gal}/[\omega_p(r_p)]_{dark\ matter}$ and weighting each scale equally in the average bias. The average scale of the mean bias is $\bar{r}_p = 4.1$ h^{-1} Mpc. The dark matter correlation function assumes a ΛCDM cosmology with $\Omega_m(0) = 0.3$ and $\sigma_8 = 0.8$. A different assumed value of σ_8 will linearly scale the bias value (e.g. a $\sigma_8 = 0.9$ will increase the absolute bias by $\sim 12\%$). The bias error is estimated from the mean bias rms measured from 10 jackknife samples, similar to the errors on r_0 and γ using power law fits.

4.2. DEEP2 *Masks and* $1/V_{max}$

When calculating $\xi(r_p,\pi)$ for a given galaxy sample, we generate random catalogs of uniformly distributed points spanning the same volume as the data. There are several observational selection effects that must be taken into account in the random catalog in order to match the spatial distribution of the data. Examples of these effects include the overall survey geometry, bright star masks, incompleteness due to DEIMOS slit design and placement, and variations in the redshift success rate due to observing conditions for each slitmask. The effects of survey geometry, data gaps, and the varying redshift success rates are all accounted for in the DEEP2 window function.

To remove the window function and any redshift selection effects, we generate a selection function from the galaxy redshift distribution and their estimated comoving distance in a ΛCDM cosmology. We smooth and spline fit the one-dimension spatial distribution such that local overdensities due to cosmic variance are removed while preserving the overall shape of the distribution. The galaxy distributions are calculated in comoving bins of $\Delta r = 0.011$ h^{-1} Mpc, and smoothing of the spline fit occurs over scales of $\Delta r = 0.03$-0.05 h^{-1} Mpc. All selection functions are checked by eye such that no power on smaller scales is retained in the smoothed selection function, which could reduce inferred correlations on those scales. Random samples are then generated from the probability distribution of the smoothed selection function. The procedure ensures that the computed correlation function statistics are not affected by the survey design or completeness of our selected galaxy samples

Although the correlation function statistics are robust, a systematic error is still imprinted on small scales where the correlation function is more likely to be incomplete due to slit collisions. Using DEEP2 mock catalogs (Yan et al. 2004), C08 found that the bias varies smoothly as a function of scale and varies in size from 25% on the smallest scales to 2% on the largest scales. We apply a correction for this systematic bias directly to the measured $\xi(r_p,\pi)$ and $\omega_p(r_p)$, and we include an additional rms error term for the correction which is measured from the mocks and added in quadrature to $\omega_p(r_p)$.

To aid in the application of our results to HOD models, we calculate the number density for each of our complete samples using the nonparametric $1/V_{max}$ method (Felten 1976) employed in previous DEEP2 studies (Blanton 2006; Zhu, Moustakas & Blanton 2009). The volume over which a given galaxy can be observed is given by

$$V_{max} = \frac{1}{3}\int d\Omega \int_{z_{min}}^{z_{max}} dz \frac{d[D_c(z)^3]}{dz} f(z), \qquad (7)$$

where $D_c(z)$ is the comoving distance and a spatially flat universe (Hogg 1999), $d\Omega$ is the solid angle of sky covered in the survey, and $f(z)$ is the probability that a given galaxy is targeted and a successful redshift is produced in a given DEEP2 mask. We calculate $d\Omega$ using the same DEEP2 masks as those used in our clustering analysis, which excludes regions of bright stars and accounts for mask edges, and we find that the integrated survey area covered in our slit masks is 2.54 deg^2.

The DEEP2 redshift success rate, $f(z)$, is a function of both R-band magnitude and restframe color; these are discussed in detail in Newman et al. (2012) (see also Blanton 2006, Willmer et al. 2006, and Zhu, Moustakas & Blanton 2009). For each observed galaxy, we generate 1200 simulated galaxies with similar observational properties between z_{min} and z_{max} and calculate k-corrected magnitudes for each simulated redshift. We then apply the selection function $f(z)$ to these simulated galaxies and produce a fraction which is multiplied by the comoving volume to produce V_{max}.

Once V_{max} is obtained, we calculate the effective number of galaxies in the comoving volume,

$$N_{eff} = \left[\sum_i \frac{1}{(V_{max})_i}\right]^2 / \left[\sum_i \frac{1}{(V_{max})_i^2}\right], \qquad (8)$$

and divide by the comoving volume between z_{min} and z_{max} to derive the number density, n. Upper and lower limits for n are computed by assuming a Poisson error distribution with approximations provided by Gehrels (1986). However, because DEEP2 is a small area survey, cosmic variance (σ_{cv}) will be a significant source of error in the number density. Following Zhu, Moustakas & Blanton (2009), we calculate the variance in number density from each of the four DEEP2 fields and report the estimated σ_{cv} along with each of our samples. In selected stellar mass cases where DEEP2 is complete, we have cross-checked our number densities with the published galaxy mass function between $0.75 < z < 1.0$ given in Bundy et al. (2006) and find good statistical agreement with their measurements.

5. GALAXY CLUSTERING RESULTS

5.1. *Clustering Dependence on Stellar Mass*

Results for the two-dimensional correlation function, $\xi(r_p,\pi)$, as a function of stellar mass are shown in Figure 8 for the $0.74 < z < 1.4$ blue galaxy samples. The figure shows contours of constant correlation strength for three bins in stellar mass ranging from $9.9 < \log(M_*/M_\odot) < 10.8$
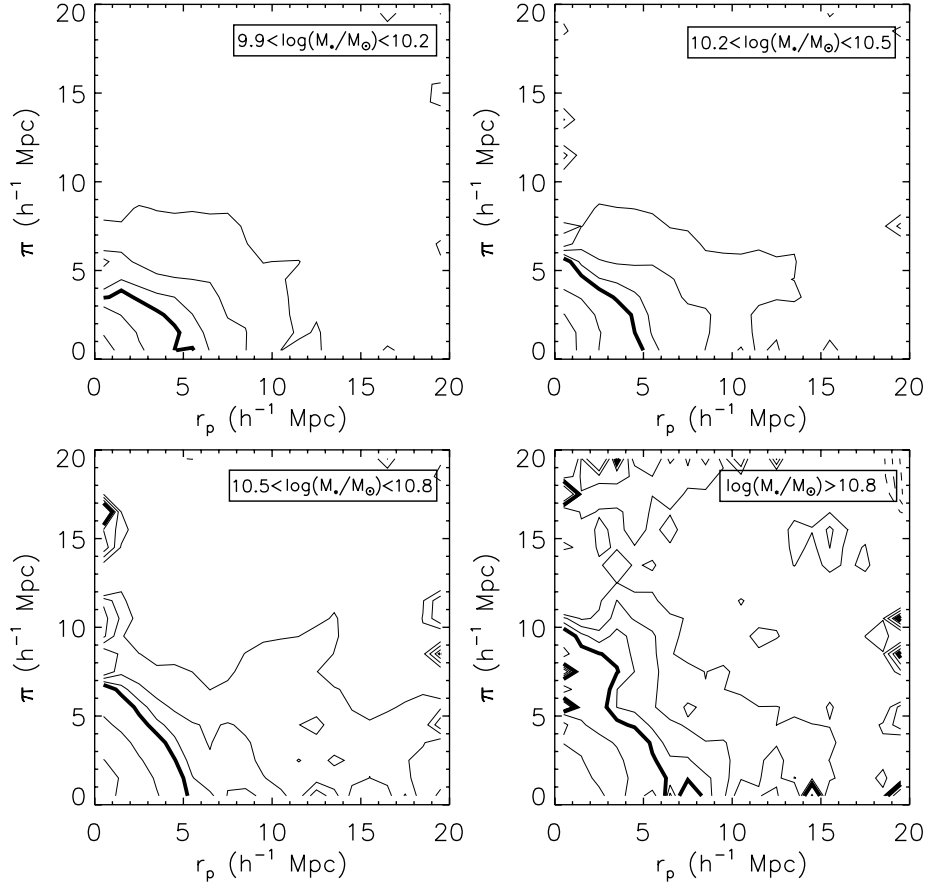
FIG. 8.— Contours of constant correlation strength for the two-dimensional correlation function, $\xi(r_p, \pi)$, for blue galaxies with $0.74 < z < 1.4$ binned by stellar mass. The contour lines correspond to correlation amplitudes of 0.25, 0.5, 0.75, 1.0, 2.0, and 5.0, with $\xi(r_p, \pi) = 1$ shown as a thick line. The number of galaxies in each bin is as follows: 4774 (upper left), 4279 (upper right), 2435 (lower left), and 1134 (lower right). The contours have been smoothed by a 1×1 h^{-1} Mpc boxcar for clarity in the figure.

and a fourth sample with a lower stellar mass threshold of $\log(M_*/M_\odot)$¿10.8 (lower right panel). In the lowest stellar mass bin, $\xi(r_p, \pi)$ is relatively symmetric both across and along the line of sight, while at higher stellar masses there is an increasing asymmetry in $\xi(r_p, \pi)$. At all masses there is evidence of a compression along the line of sight on large scales, due to coherent infall into gravitational potential wells known as the "Kaiser effect" (Kaiser 1987). Redshift-space distortions on small scales ("Fingers of God") also increase dramatically with stellar mass, indicating that high-stellar-mass blue galaxies have greater virial motions and therefore are in systems with larger halo mass. These results mirror those of C08, who found a similar increase in redshift-space distortions with increasing luminosity (see their Figure 7).

To mitigate the effects of these redshift-space distortions in our clustering analysis, we integrate the two-dimensional correlation function along the line of sight to project the clustering signal onto the r_p axis. This results in the projected correlation function, $\omega_p(r_p)$, which we show for color-independent mass threshold samples in Figure 9 and color-dependent mass threshold samples in Figure 10. We also plot the projected dark matter correlation function (Smith et al. 2003) generated for a ΛCDM universe ($\sigma_8 = 0.8$) at a mean redshift similar to that of the galaxy samples ($z = 0.9$). In all cases, $\omega_p(r_p)$ is

consistent with a power law on scales larger than $r_p > 1$ h^{-1} Mpc where the clustering of galaxies in independent halos (e.g the two-halo term) dominates the correlation function.

On scales of $r_p \leq 0.3$ h^{-1} Mpc, we find a departure from a single power law for the highest stellar masses in the color-independent sample (Figure 9) and at similar masses in red galaxies (left side of Figure 10). The departure on small scales is seen more clearly in Figure 11, where we divide out the large-scale power law fit over 1-10 h^{-1} Mpc and plot the relative correlation function for red and blue galaxy mass samples. For clarity, the figure shows these relative correlation functions with an offset of 0.3 dex between different stellar mass samples.

To determine the significance with which the observed clustering on small scales is a departure from the large-scale behavior, we perform a t-test between the relative large-scale and small-scale clustering amplitude (Figure 11). For each jackknife subsample of a given galaxy sample, we fit a power law over large scales with r_p=1-10 h^{-1} Mpc and ratio the correlation function averaged over $r_p \leq 0.3$ h^{-1} Mpc to the best-fit power law averaged over the corresponding small scales. We then compute the mean and standard deviation among the 10 jackknife sample ratios and compute a t score in which the null hypothesis ratio value is 1. Finally, we compute the
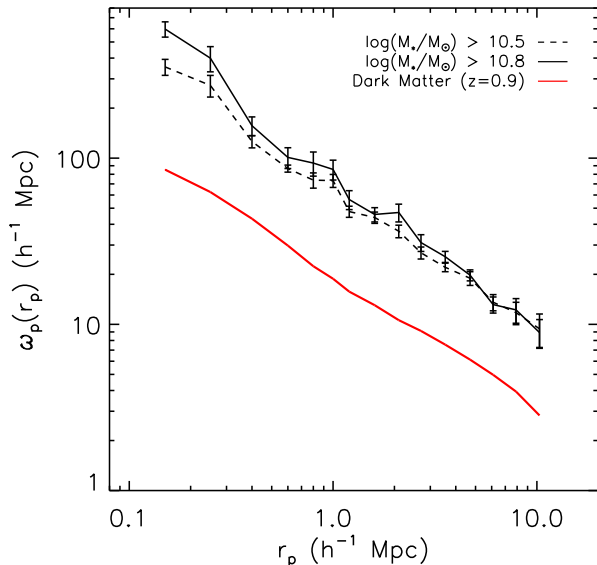
FIG. 9.— The projected correlation function, $\omega_p(r_p)$, for color-independent galaxy samples selected by stellar mass thresholds and limited to $z<1.05$. The plot shows the two highest mass threshold samples with $\log(M_*/M_\odot)>10.5$; the highest mass sample is complete for both red and blue galaxies and the lower mass sample is slightly incomplete for red galaxies beyond $z¿0.9$. The projected clustering of dark matter (solid, red line) is generated from the prescription of Smith et al. 2003 and shown for a redshift of $z=0.9$, which is similar to the mean redshift of the galaxy samples.

corresponding p-value drawn from a t-distribution with 9 degrees of freedom. Assuming that there is minimal correlated error between $r_p{\leq}0.3$ h^{-1} Mpc and $r_p > 1$ h^{-1} Mpc, this procedure encapsulates the error associated with both the large-scale power law fit and the covariance of $\omega_p(r_p)$ on small scales.

For red galaxies with $10.5<\log(M_*/M_\odot)<11.0$, the t-test produces a p-value of $p=0.005$, meaning that a small-scale deviation as large as that observed or larger would occur only 0.5% of the time if there were in fact no true deviation. Red galaxies with $\log(M_*/M_\odot)>11.0$ have a small-scale deviation from the large-scale power law fit with $p = 0.042$, a significant deviation at the $p < 0.05$ significance level. The lower significance in the higher mass galaxy sample is due in part to larger correlated variation in the large-scale power law slope γ in the jackknifed samples. For blue galaxies (right side of Figure 11), we find no statistically significant increase in clustering on small scales relative to large scales at any stellar mass probed in this study. The difference in the relative correlation function amplitude between red and blue galaxy samples on small scales could indicate a change in the central-to-satellite fraction and/or a change in the halo mass distribution in the halo mass function (Zheng et al. 2009). We will further discuss the physical interpretation of this result in Section 6.4.

The left panel of Figure 12 shows the measured correlation length, r_0, when fitting $\omega_p(r_p)$ with a power law model of $\xi=(r/r_0)^{-\gamma}$. As the slope of the correlation function, γ, can be covariant with r_0, we fix $\gamma=1.6$ to study the trends in r_0 with stellar mass. We find a strong positive correlation between r_0 and stellar mass for $\log(M_*/M_\odot)<11.0$ for blue, red, and color-independent galaxy samples. At $11.0<\log(M_*/M_\odot)<11.5$, the clus-

tering length appears to level off at $r_0 \sim 5$ h^{-1} Mpc for all colors and does not depend on stellar mass, within the errors. The r_0 results could indicate that high-stellar-mass blue galaxies at $z>1$ are precursors to similar mass red galaxies at $z<1$, as they likely reside in similar mass halos. We note that the DEEP2 sample has poor constraints for *all* stellar masses above $\log(M_*/M_\odot)>11.5$; the survey volume is not large enough to robustly sample the rarest, most massive galaxies. The measured values of r_0, γ, and the absolute bias for each stellar mass sample are given in Tables 1 and 2. By design, the absolute bias has a similar trend to r_0 where the bias increases with stellar mass. We find no significant trend between the best fit correlation slope γ and stellar mass.

For the threshold samples in Table 1, we also estimate the minimum and mean halo mass using the measured large-scale galaxy bias and the halo mass function for central galaxies (Sheth & Tormen 1999; Jenkins et al. 2001), modified to accommodate the increased frequency of satellites at low halo mass (see the Appendix of Zheng et al. (2007) for details). For each galaxy sample, we use the halo mass function calculated for the mean redshift of the sample in a ΛCDM cosmology ($\sigma_8=0.8$), and we assume a satellite fraction of $\sim 17\%$ as measured for DEEP2 L^* galaxies (Zheng et al. 2007). We caution that the minimum and mean halo masses are intended as estimates in lieu of a full HOD model fit to $\omega_p(r_p)$, which we reserve to a future study. Table 1 shows that the mean halo mass ranges from $<\log(M_{\rm halo})>=$ 12.3 $h^{-1}M_\odot$ in the lowest stellar mass blue galaxy sample to $<\log(M_{\rm halo})>\sim 13$ $h^{-1}M_\odot$ at the highest stellar masses. This mass range is particularly interesting as halo mass assembly models predict that galaxies at $z=1$ transition from slow clustering growth below $10^{12}M_\odot$ to near exponential clustering growth above 10^{13} $M_\odot$ (Moster et al. 2010; Leauthaud et al. 2012). Although the halo masses presented here are estimates, we expect that they will help constrain the stellar-mass/halo-mass relationship in this important mass range at $z \sim 1$.

5.2. *Clustering Dependence on Star Formation Rate*

We now investigate how clustering properties depend on SFR using the SFR-selected galaxy samples described in Section 3.2. Because complete samples of red and blue galaxies probe vastly different SFR ranges, we consider only galaxy samples separated by color (see Figure 5). Following the same procedure as with stellar mass, we investigate trends in the redshift space distortions for blue galaxies as a function of SFR by studying $\xi(r_p,\pi)$. We find that blue galaxies at all SFRs display "Kaiser infall" on large scales, and all samples have relatively small "Fingers of God" on small scales. This implies that large-scale infall dominates the $\xi(r_p,\pi)$ signal in our SFR samples and contrasts with the significant redshift-space distortions seen as a function of stellar mass. The lack of "Fingers of God" indicates that the SFR samples must span a broader range of stellar masses than mass-selected samples, thus diluting the strong "Fingers of God" seen in the latter.

Turning to the projected correlation function, Figure 13 shows $\omega_p(r_p)$ for two SFR threshold levels ranging from $-0.1<\log(\psi)<0.4$ $M_\odot$ yr^{-1} for red galaxies and
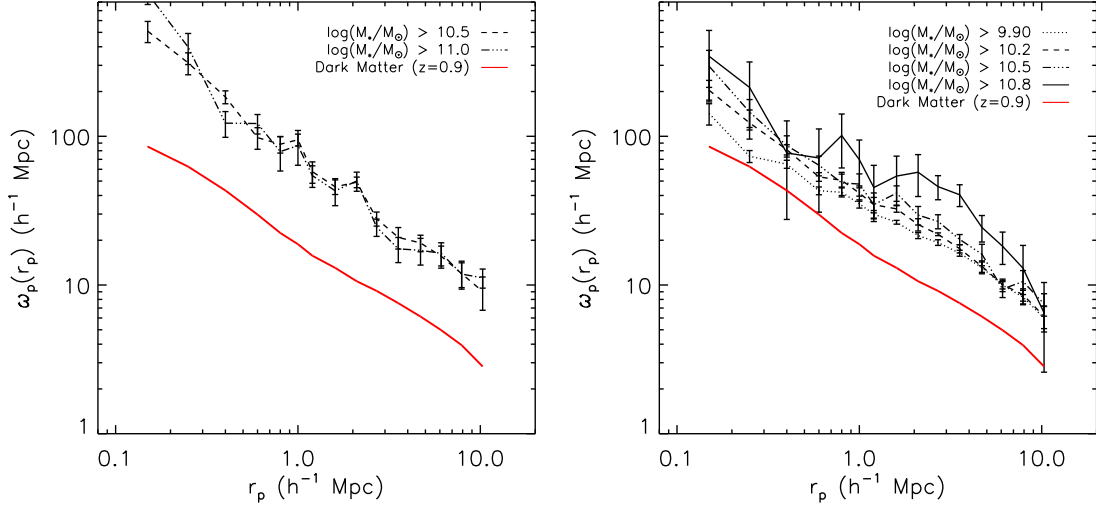
FIG. 10.— The projected correlation function, $\omega_p(r_p)$, for color-dependent galaxy samples selected by stellar mass. Stellar mass threshold samples for red galaxies at $z<1.05$ are shown on the left, while stellar mass threshold samples for blue galaxies at $z<1.4$ are shown on the right.
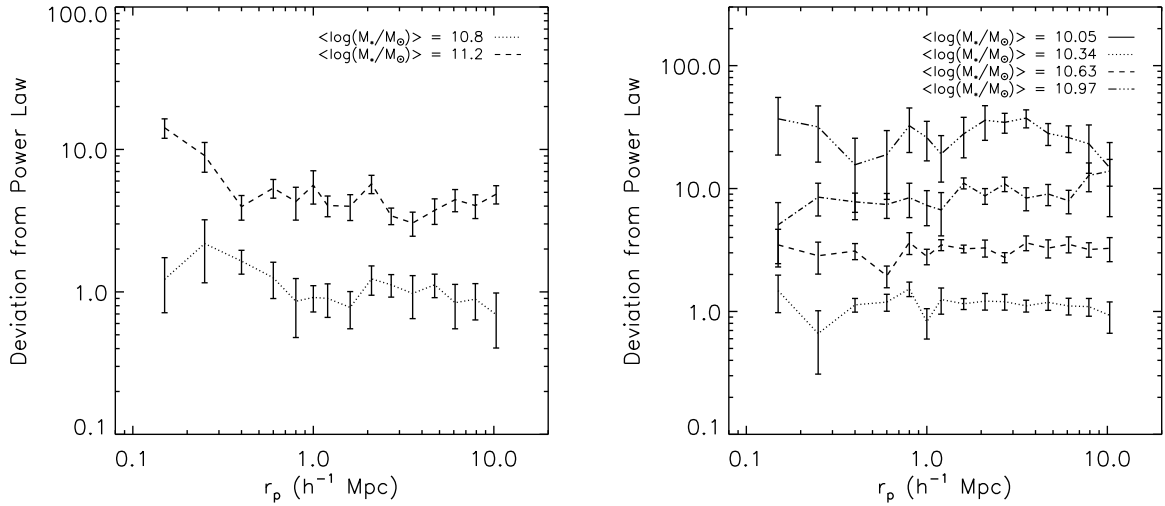

FIG. 11.— The relative deviation in $\omega_p(r_p)$ from the best-fit power law for galaxy samples separated by red (left) and blue (right) restframe color and binned by stellar mass. The power law is fit to $\omega_p(r_p)$ on scales of 1-10 h^{-1} Mpc. Each sample is offset by an arbitrary 0.3 dex for clarity in the figure. The mean deviation between the relative small-scale clustering below $r_p \leq 0.3$ h^{-1} Mpc and large-scale clustering between $0.4<r_p<10.5$ h^{-1} Mpc is significant in red galaxies at the $p<0.1$ level for $10.5<\log(M_*/M_\odot)<11.0$ and $p<0.001$ level for $\log(M_*/M_\odot)>11.0$. We find no significant increase in small-scale clustering for any of the blue galaxy mass samples beyond the best-fit large-scale power law.

three SFR threshold levels between $0.75<\log(\psi)<1.25$ $M_\odot$ yr^{-1} for blue galaxies. The samples shown are restricted to $z<1.05$ for a direct comparison between red and blue galaxy samples within the same volume. We find that the clustering amplitude changes much less as a function of SFR within the red or blue sample compared to the difference in amplitude between the red and blue samples. Blue galaxies with higher SFR have higher clustering amplitude, while there is no detected difference in clustering for the two red galaxy samples as a function of SFR, within the errors. Figure 14 shows the deviation of $\omega_p(r_p)$ from a power law fit on scales of 1-10 h^{-1} Mpc for red (left) and blue (right) galaxies binned by SFR. For all samples with $\log(\psi)<1.5$ $M_\odot$ yr^{-1}, there is no

significant deviation from a power law on small scales ($r_p \leq 0.3$ h^{-1} Mpc). For the highest SFR blue galaxies with $\log(\psi)>1.5$ $M_\odot$ yr^{-1}, however, we detect a factor of seven increase in the mean clustering amplitude below $r_p \leq 0.3$ h^{-1} Mpc relative to the large-scale power law fit. Performing the same t-test as was done for stellar mass, the excess clustering signal has a p-value of $p=0.038$ and therefore is significant at the $p<0.05$ level.

The measured r_0 values for color-separated galaxy samples binned by SFR are shown in the center panel of Figure 12. The clustering scale length increases with increasing SFR for blue galaxies and is constant for red galaxies as a function of SFR, within the measurement error. However, blue galaxies with the highest SFR have clustering amplitudes similar to red galaxies, suggest-
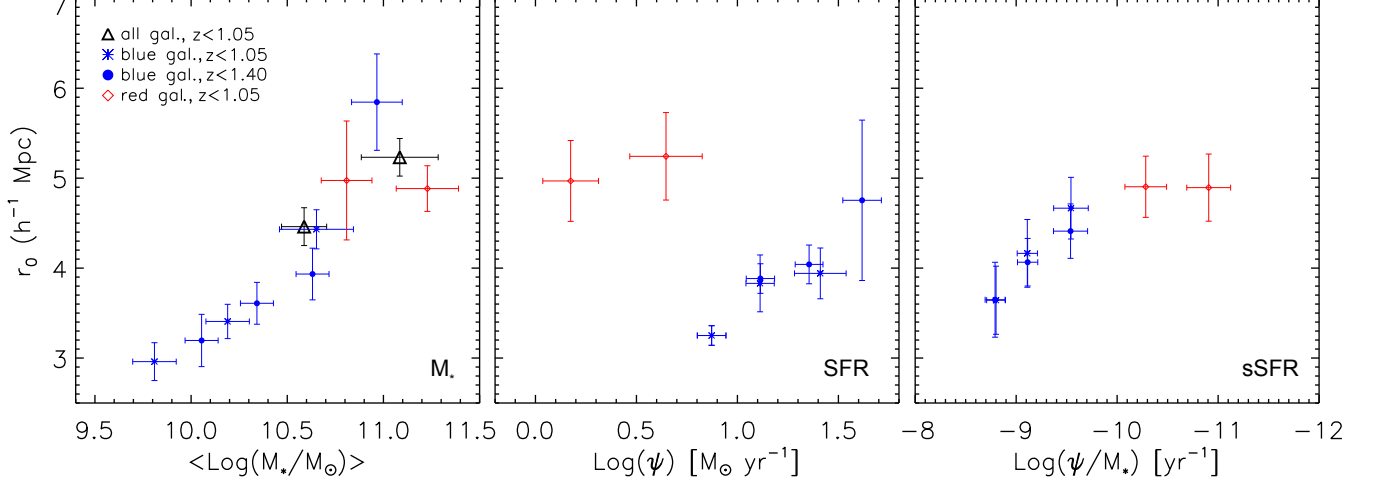
FIG. 12.— The clustering scale length, r_0, measured by fitting a power law to $\omega_p(r_p)$ over linear scales of 1-10 h^{-1} Mpc. For this figure, the power law slope is fixed to $\gamma=1.6$ so as to remove degeneracies between r_0 and γ. The scale lengths are measured for galaxy samples in stellar mass (left), SFR (center), and sSFR (right) as described in Sections 3.1-3.3. Vertical error bars are calculated from the rms scatter of r_0 fit from 10 jackknifed sub-samples in each data bin, and horizontal error bars represent the rms scatter for each bin of selected galaxy sample values. All measured values of absolute bias, r_0, and γ are given in Tables 1-6.
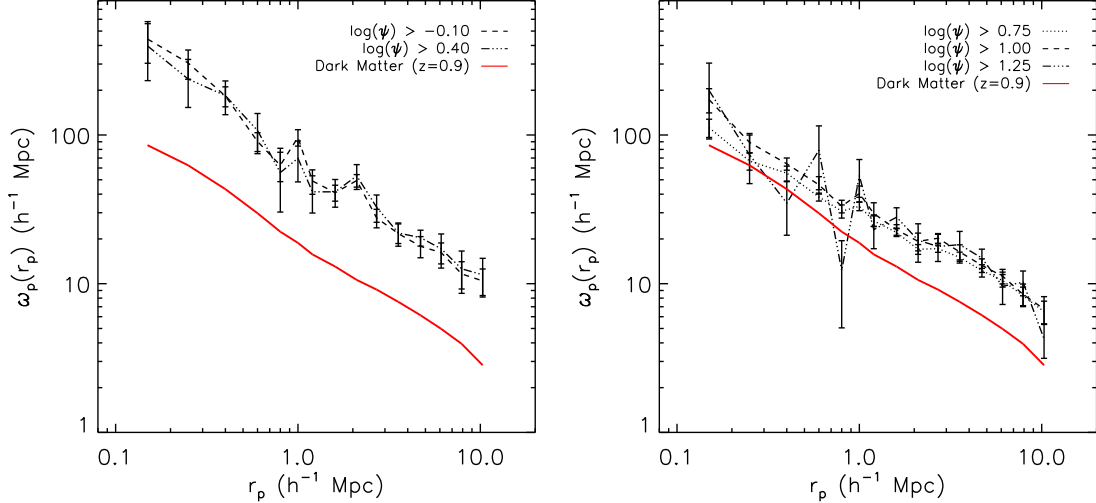

FIG. 13.— The projected correlation function, $\omega_p(r_p)$, for red (left) and blue (right) galaxy samples as a function of SFR threshold, limited to $z<1.05$. The dark matter projected correlation function is shown for $z=0.9$, near the mean redshift of all galaxy samples.

ing that they occupy the same mass halos at these redshifts. The overall trends in clustering amplitude agree with $z \sim 1$ environment studies performed in CP08, who found that the galaxy overdensity increases at both extremes of galaxy SFR.

Tables 3 and 4 list the r_0, γ, and bias values for each SFR sample, and Table 3 further lists the minimum and mean halo mass estimated for the SFR threshold samples. We note that while there is a significant rise in the clustering amplitude on small scales for the highest SFR galaxies, there is no trend between SFR and γ, within the errors. The red galaxy SFR samples, which are just as clustered on large scales as the highest-SFR blue galaxy sample, have a consistent clustering slope as all of the blue SFR samples, though the errors on the slope are large.

Interestingly, when comparing the stellar mass and SFR samples in Figure 12, the $\log(\psi)>1.5$ $M_\odot$ yr^{-1} blue

galaxy sample has similar correlation lengths as the high-stellar-mass red galaxy samples. Further, as shown in Figures 11 and 14, we see similar enhanced clustering on small scales relative to the best fit large-scale power law behavior in these galaxy samples. The similarities between high-SFR blue galaxies and high-stellar mass red galaxies on *both* large and small scales indicates that they are found in similar mass halos, perhaps linked to a shared star formation history, with high-SFR blue galaxies evolving to high-stellar mass, low-SFR red galaxies at later epochs after the star formation in the galaxy is quenched.

5.3. *Clustering Dependence on Specific Star Formation Rate*

We also measure galaxy correlation properties as a function of specific SFR (sSFR). The sSFR is the inverse of the star-formation timescale of a galaxy. In secular evolution scenarios, the measured sSFR timescale is
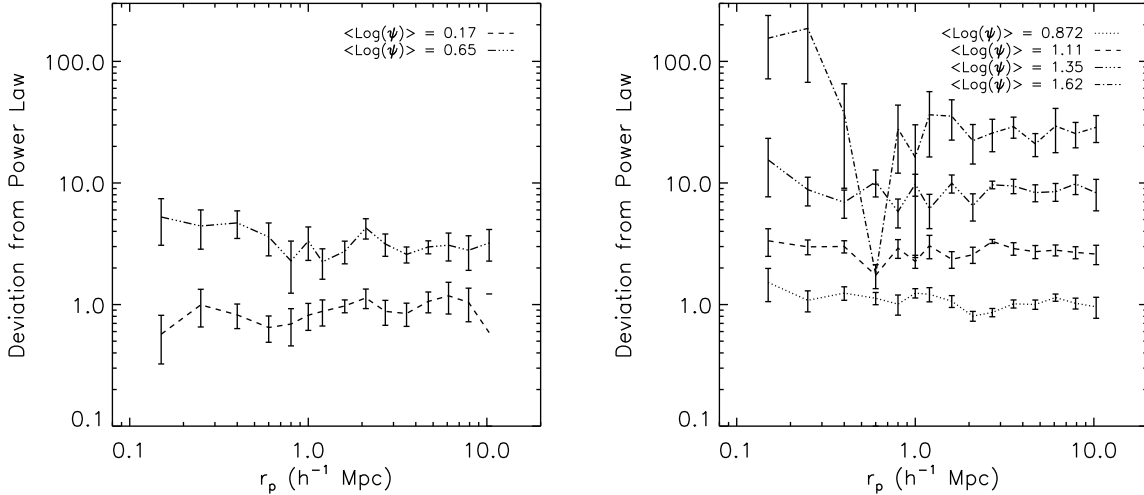
Fig. 14.— The relative deviation in $\omega_p(r_p)$ from the best-fit power law for red (left) and blue (right) galaxy samples binned by SFR. Similar to stellar mass in Figure ref:relmasscorrcolor, the power law is fit to $\omega_p(r_p)$ on scales of 1-10 h^{-1} Mpc, and each sample is offset by an arbitrary 0.3 dex in the figure for clarity. We find evidence of enhanced small-scale clustering in the highest-SFR blue galaxy sample but not for either red galaxy sample.

proportional to the existing stellar mass relative to the amount of cold interstellar gas available for production of stars. Shorter timescales indicate rapid star formation from large, cold interstellar gas reserves and vice versa for longer timescales. As shown in Figure 2, sSFR is strongly correlated with restframe color as it reflects the star formation history of the aggregate stellar population within a galaxy.

Figure 15 shows $\omega_p(r_p)$ for the color-dependent sSFR threshold samples described in Section 3.3. The sSFR samples are complete between $0.74 < z < 1.05$ for $M_B < -20.5$ blue galaxies and $M_B < -21.0$ red galaxies. In general, lower sSFR samples are more clustered than higher sSFR samples, which is expected given the strong correlation between clustering and galaxy color (C08). Figure 16 shows the deviation from the best fit power law for samples binned by sSFR. We find that for the lowest sSFR galaxies in *both* red and blue samples, $\omega_p(r_p)$ deviates significantly on small scales ($r_p \lesssim 0.3$ h^{-1} Mpc) relative to the large-scale power law fit. There is a factor of 4 increase in the small-scale clustering amplitude for $-10.6 < \log(\psi/M_*) < -9.9$ red galaxies and a similar increase for $-8.95 < \log(\psi/M_*) < -8.6$ blue galaxies. The t-test for both these samples produce p-values of $p = 0.013$ and $p = 0.018$, respectively. Additionally, we find that the $0.74 < z < 1.4$ blue galaxy sample with $M_B < -21.0$ and $-8.95 < \log(\psi/M_*) < -8.6$ also deviates from the large-scale power law fit by an average factor of 7 and has a highly significant increase in clustering ($p = 2.8 \times 10^{-5}$) on $r_p \lesssim 0.3$ h^{-1} Mpc scales. The enhanced small-scale clustering indicates that the satellite fraction is related to how efficiently galaxies within a single halo, regardless of restframe color, process gas and produce stars. We discuss the implications of this result further in Section 6.

The right panel of Figure 12 shows the best fit r_0 values for galaxy samples binned by sSFR. The clustering length rises for blue galaxies with lower sSFR values and is constant for red galaxies with $\log(\psi/M_*) < -10$. Both red and blue galaxies with $-10.5 < \log(\psi/M_*) < -9.5$ have

similar clustering lengths and therefore likely occupy similar mass dark matter halos. The correlation slope, γ, also roughly trends towards higher values for lower sSFRs, although the trend is not highly significant given the errors. Tables 5 and 6 list the r_0, γ, and bias values for each sSFR sample. Table 5 further records the minimum and mean halo mass estimated for the sSFR threshold samples.

6. DISCUSSION

The primary goal of this work is to measure the clustering properties of complete $z \sim 1$ galaxy samples selected by stellar mass, SFR, and sSFR . We present a macroscopic view of our results in this section. To facilitate this discussion, we separate our findings into small- and large-scale behavior at $r_p \sim 1$ h^{-1} Mpc, which roughly corresponds to the transition between the one and two-halo terms in HOD models. We first discuss the large-scale clustering results, including a comparison with previous work and relevant environment studies, and then discuss the small-scale clustering results.

6.1. *Large-scale Clustering Behavior*

The projected 2PCFs measured in this study allow us to quantify the relationship between galaxy clustering and stellar mass and SFR at $z \sim 1$. We first discuss how our power law fits to the projected correlation function on large scales compare with other studies. In the left hand panel of Figure 17, we compare our r_0 results for color-independent, stellar mass threshold samples to results from NMBS (Wake et al. 2011) and VVDS (Meneux et al. 2008) at $z \sim 1$. Wake et al. calculated the angular correlation function of galaxy samples as a function of stellar mass using NMBS photometric redshifts in portions of the COSMOS and AEGIS fields (Scoville et al. 2007; Davis et al. 2007; van Dokkum et al. 2009), covering 0.4 deg^2 in total. For NMBS, the angular correlation function is fit at $0.9 < z < 1.3$ over scales of $\sim 0.05 - 10h^{-1}$ Mpc with a fixed $\gamma = 1.6$. The DEEP2 results shown also
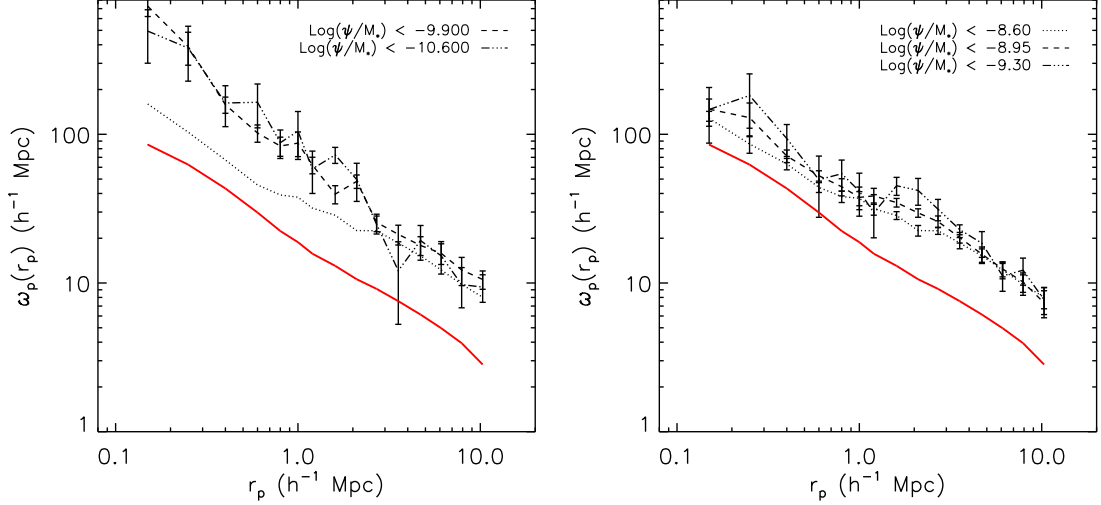
FIG. 15.— The projected correlation function, $\omega_p(r_p)$, for red (left) and blue (right) galaxy samples selected using sSFR thresholds between $0.74 < z < 1.05$. The dark matter projected correlation function is shown for $z=0.9$, near the mean redshift of all galaxy samples. The dotted line in the left panel corresponds to $\omega_p(r_p)$ for blue galaxies with $\log(\psi/M_*) < -8.6$ yr^{-1}, shown in the right panel.
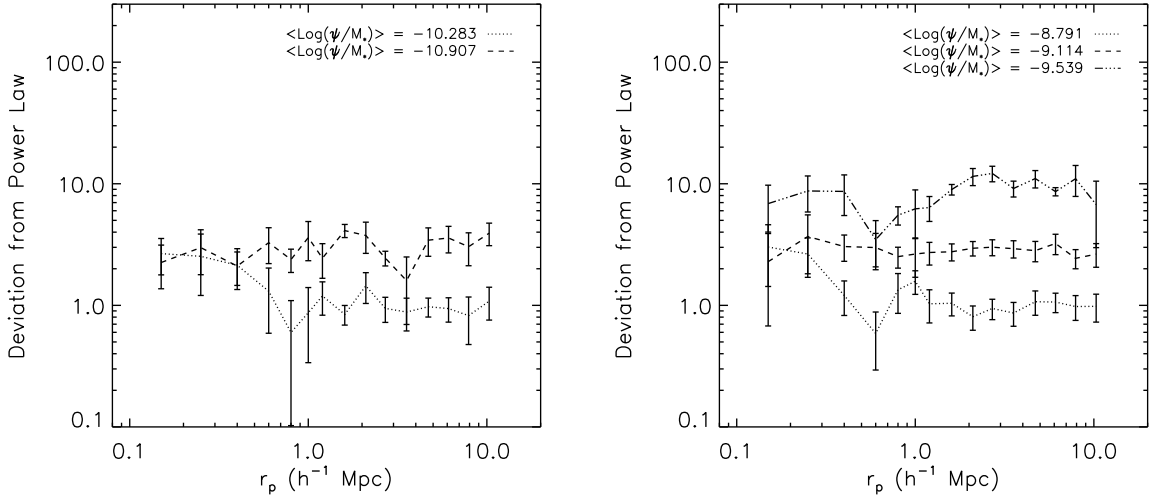

FIG. 16.— The relative deviation in $\omega_p(r_p)$ from the best-fit large-scale power law for red (left) and blue (right) galaxy samples binned by sSFR. A significant rise in the clustering amplitude is seen on small scales for the highest sSFR samples for both red and blue galaxies.

have a fixed $\gamma = 1.6$ to facilitate comparison and remove degeneracies. Meneux et al. used spectroscopic redshifts from the VVDS-Deep field (Le Fevre et al. 2003) to calculate $\omega_p(r_p)$ over 0.49 deg^2, fitting r_0 over r_p=0.1-21 h^{-1} Mpc. While the VVDS results also allow γ to vary in the fits, a slightly higher value of $\gamma = 1.8$ is typical for their 2PCF data. We find good agreement with the VVDS clustering amplitudes; both VVDS and DEEP2 results are less clustered than the NMBS results, though the difference is not significant given the NMBS errors. This may be due to cosmic variance within the NMBS $z = 1.1$ sample, where independent correlation functions in the COSMOS and AEGIS samples are quite different on large scales (although they statistically agree given the size of the errors, see their Figure 2).

We also note that the DEEP2 stellar mass threshold sample with galaxies of all colors above $\log(M_*/M_\odot) > 10.5$ is somewhat incomplete for red galax-

ies at the low mass end beyond $z > 0.9$. As stated in Section 3.1, the red galaxy incompleteness between $10.4 < \log(M_*/M_\odot) < 10.8$ is estimated to be $\sim 20\%$ between $0.74 < z < 1.05$. As the clustering amplitude at a fixed stellar mass appears to be similar for red and blue galaxies above $\log(M_*/M_\odot) > 10.8$, we expect the clustering strength for the $\log(M_*/M_\odot) > 10.5$ threshold sample to be relatively unaffected by the red galaxy incompleteness. If we assume that r_0 for the color-independent sample behaves as a weighted average between the red and blue galaxy samples (given in Table 1), then increasing the number of red galaxies by 20% would only increase the clustering strength by $\sim 1\%$, much less than the quoted error.

We further compare our best fit clustering amplitudes to similar measurements in the local universe from SDSS (Li et al. 2006). The center panel of Figure 17 shows r_0 for color-independent, binned stellar mass samples in

SDSS[7]. As Li et al. (2006) did not measure r_0 from their projected 2PCFs, we fit their $\omega_p(r_p)$ data over r_p=1-10 h^{-1} Mpc scales in a similar manner to our DEEP2 data. The Li et al. (2006) $\omega_p(r_p)$ data is drawn from a sample of $\sim 200,000$ SDSS galaxies with an average statistical error of 5% per measured scale over the fitted scale range and does not account for the full covariance between measured scales. Therefore, our power law fits to their published data have a small 1% statistical error for each stellar mass sample and may not be fully representative of the true error in the SDSS $\omega_p(r_p)$ data. Zehavi et al. (2011) estimate the r_0 error to be $\sim$5% from jackknifed samples of galaxy luminosity bins in SDSS, and therefore our conclusions comparing clustering amplitudes should be relatively robust. The same plot also shows the three most complete stellar mass samples in VVDS. Because the VVDS-Deep data becomes incomplete for blue galaxies below $\log(M_*/M_\odot)$<10, the measured clustering amplitude is systematically biased to lower values of r_0. At most, Meneux et al. (2008) calculated that the (9.5<$\log(M_*/M_\odot)$<10.0) stellar mass bin underestimates the clustering amplitude by 10% relative to mock catalogs. DEEP2 color-independent stellar mass samples are limited to $\log(M_*/M_\odot)$>10.5, while the VVDS data extends to somewhat lower stellar mass with an $I_{\rm AB}$=24 magnitude limit. Again, we find excellent agreement in clustering strength between DEEP2 and VVDS at $z \sim 1$, both of which have significantly lower r_0 values than local SDSS galaxies for all stellar masses probed. At a fixed stellar mass, we estimate that the clustering amplitude in color-independent samples has increased by roughly 35% from $z = 1$ to $z = 0.1$.

The right panel of Figure 17 shows r_0 for stellar mass selected samples separated by red and blue restframe colors in both SDSS and DEEP2. On large scales, we find that blue galaxies are somewhat more clustered ($\approx 15\%$) locally when compared to $z \sim 1$, although the r_0 values are completely consistent at the highest stellar mass, $\log(M_*/M_\odot)$=11.25. Red galaxies at the same stellar mass, however, are much more clustered locally than at $z \sim 1$. We interpret this to mean that lower stellar mass blue galaxies have much of their current halo mass in place by $z \sim 1$, and therefore there is little evolution in the clustering amplitude over the last 8 Gyrs. However, the halos that host massive red galaxies, which are more likely to be central galaxies, accumulate fractionally more halo mass relative to their existing stellar mass over the same span of cosmic time. This effectively causes the clustering amplitude to increase at a fixed stellar mass and therefore become more clustered on large scales at recent epochs. These results support stellar-halo mass assembly history models where lower stellar mass blue galaxies have most of their final halo mass in place at $z \sim 1$ but continue to add to their stellar mass, while higher stellar mass red galaxies form most of their final halo mass at z<1 but have little evolution in their stellar mass (Zheng et al. 2007; Conroy & Wechsler 2009; Coupon et al. 2012).

Our clustering measurements also agree with the blue

and red luminosity-dependent clustering results of C08, who found that red galaxies are more clustered than blue galaxies at $z = 1$ at the same luminosity (which corresponds to a lower stellar mass for blue galaxies compared to red) and less clustered than their local red counterparts at the same luminosity ($r_0 \approx 5$ h^{-1} Mpc at $z \sim 1$ versus $r_0 \approx 6$ h^{-1} Mpc locally, see Figure 11 in C08). Further, the results in the lower red galaxy stellar mass bin are consistent with the results found in C08, given the errors. We find a slightly larger clustering difference between $z \sim 1$ red galaxies selected by stellar mass and those at $z \sim 0.1$, using fits to the Li et al. $\omega_p(r_p)$ data. We note that our highest stellar mass red galaxy sample is a *threshold* sample limited by the total probed volume in DEEP2 volume. This upper stellar mass limit will not include the rarest, most massive galaxies that would be present in the larger SDSS volume within an equivalent stellar mass range. Another concern is that less massive star-forming galaxies that have been reddened by dust could be included in red galaxy samples, which may cause r_0 to be underestimated. Results from the PRIMUS survey (Zhu et al. 2011) show that such heavily reddened star-forming galaxies are rare at the bright end of the red sequence ($\leq 10\%$) at intermediate redshift and therefore should have relatively little weight in the large-scale 2PCF amplitude.

There are relatively few studies that have explored galaxy clustering at $z \sim 1$ as a function of stellar mass, SFR, and sSFR to which we can compare directly. However, recently Lin et al. (2012) performed an angular clustering analysis of BzK-selected star-forming galaxies at $z \sim 2$. They also found that the measured clustering scale length increases strongly with increasing stellar mass ($\log(M_*/M_\odot)$>9), increasing SFR ($\log(\psi)$>0.5), and decreasing sSFR ($\log(\psi/M_*)$<−8.6), in good agreement with the trends found here. However, because we have restricted our blue galaxy sSFR samples to M_B<−20.5 and $\log(\psi/M_*)$<−8.6 for completeness to z<1.4, we do not probe higher values of sSFR beyond z>1 in this study. We therefore cannot confirm the existence of a turnover in the clustering behavior at higher values of sSFR as presented in Lin et al. (2012).

We can also compare our results as a function of sSFR to those of Li et al. (2008), who measured $\omega_p(r_p)$ for a large sample of SDSS galaxies with sSFRs ranging from -11<$\log(\psi/M_*)$<-9. To facilitate this comparison, we follow Li et al. and compute the best fit $\xi(r)$ power law from 10 jackknifed samples of our $\omega_p(r_p)$ data as a function of sSFR and normalize to a constant power law of $\xi(r)_{\rm pow} = (r/5$ h^{-1} Mpc$)^{-1.8}$. As we fit $\omega_p(r_p)$ over scales 1-10 h^{-1} Mpc in each jackknife sample, we evaluate the power law $\xi(r)_{\rm fit}$ for the unweighted mean values of r_0 and γ at a fixed scale of 5 h^{-1} Mpc and plot the ratio of the 2PCFs as a function of sSFR (see Figure 18). Compared to Li et al. (2008) (also at $r_p = 5$ h^{-1} Mpc), we find good qualitative agreement with the trend seen for local clustering results. At $\log(\psi/M_*)$>-9.5, there is a significant trend to lower clustering amplitudes at higher sSFR, while the large-scale clustering amplitude is relatively independent of sSFR at $\log(\psi/M_*)$<−9.5. At $\log(\psi/M_*)$<−10.5 we do not see a rise in the large-scale clustering amplitude, as is seen locally. The trend of increased clustering at lower sSFRs should be expected
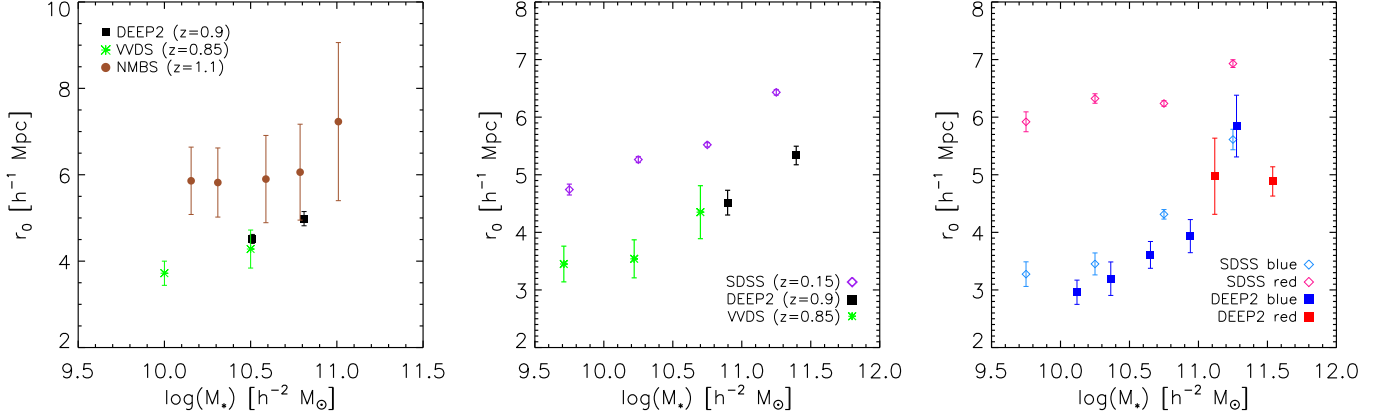
FIG. 17.— (left) Clustering scale length, r_0, measured from color-independent stellar mass threshold samples in DEEP2 (black square), VVDS data (green star) from Meneux et al. (2008), and NMBS data (brown circle) from Wake et al. (2011). Data point locations indicate the lower mass threshold limit imposed on each sample. The Wake et al. measurements use NIR photometric redshifts to compute the angular correlation function at $0.9 < z < 1.3$. Both VVDS and DEEP2 have a lower clustering amplitude than the NMBS at $\log(M_*) < 11.0$ $h^{-2} M_\odot$, although the errors from the 0.4 deg^2 NMBS survey are relatively large in comparison. (center) r_0 resulting from power law fits to color-independent stellar mass bin samples in SDSS (Li et al. 2006), VVDS, and DEEP2. Fits are performed over $r_p = 1\text{-}10$ h^{-1} Mpc in DEEP2 and SDSS (purple diamond) while VVDS is fit over scales of $r_p = 0.1\text{-}21$ h^{-1} Mpc. All points have similar mass bin sizes of 0.4-0.5 dex, and the power law slope γ is not fixed in the $\omega_p(r_p)$ fits. The DEEP2 clustering scale lengths agree well with those from VVDS, both of which show lower clustering amplitudes at earlier times for all stellar masses probed. (right) Best fit r_0 values for restframe color-separated red and blue galaxy stellar mass bin samples in SDSS and DEEP2 for a fixed $\gamma = 1.6$ over $r_p = 1\text{-}10$ h^{-1} Mpc. DEEP2 mass bins range in size from 0.3 to 0.4 dex for blue and red galaxies, respectively. Blue galaxies in the local universe are somewhat more clustered at a given stellar mass than at $z \sim 1$, while massive red galaxies are more clustered locally.
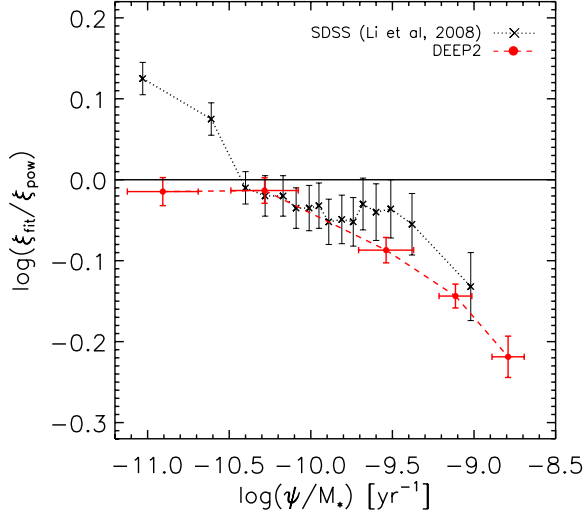

FIG. 18.— The best fit power law for $\xi(r)$ measured from the DEEP2 sSFR samples on 1-10 h^{-1} Mpc scales (red circles). The real-space 2PCF is normalized to a power law of $\xi(r)_{\text{pow}} = (r/5h^{-1} \text{Mpc})^{-1.8}$ at a fixed scale of $r = 5h^{-1}$ Mpc to match the average scale for the DEEP2 data. Li et al. (2008) produced similar measurements in SDSS at equivalent scales (black crosses). The relative trend in sSFR is similar between $z \sim 1$ and local redshifts for $\log(\psi/M_*) > -10.5$; lower clustering amplitudes are observed at progressively higher sSFR values. For $\log(\psi/M_*) < -10.5$, the $z \sim 1$ galaxies are less clustered than their local counterparts at fixed sSFR.

given the C08 results, as sSFR is highly correlated with restframe color (see right panel of Figure 2) and C08 found an increased clustering amplitude with redder colors.

Here again, as with the highest stellar mass red sample ($\log(M_*/M_\odot) > 11.0$), the sample with the lowest sSFR ($\log(\psi/M_*) < -10.6$) is a threshold sample which is limited by the DEEP2 survey volume. As the clustering

signal from the rarest galaxies cannot be measured from DEEP2 data, the clustering amplitude in this sample may be underestimated relative to larger survey volumes such as SDSS. The effect is expected to be minimal.

6.2. Clustering Amplitude and the SFR-M_* Relationship

While galaxy samples selected by SFR probe a wide range of stellar mass, stellar mass and SFR are known to be correlated (e.g., Noeske et al. 2007a) such that the mean stellar mass increases with increasing SFR. In Section 5.1, we showed that the clustering amplitude r_0 increases monotonically with stellar mass, as the amount of baryons processed into stars correlates with the halo mass. Therefore, it is possible that the change in mean stellar mass for our blue SFR samples is responsible for the observed increase in clustering amplitude with increasing SFR. Similar investigations in environmental studies (Peng et al. 2010; Sobral et al. 2010) have found little to no difference between the SFR-density and stellar mass-density relationships, indicating that the SFR-density relation could be entirely due to differences in stellar mass.

To address this question, we generate a prediction for r_0 based on the measured clustering with stellar mass using a fixed slope of $\gamma = 1.6$ (see left panel of Figure 12). We fit an exponential relation between r_0 and $\log(M_*/M_\odot)$ for binned blue galaxy stellar mass samples, finding a best fit relation of

$$r_0(M_*) = e^{2.57\log(M_*/M_\odot)-27.1} + 2.88. \quad (9)$$

We then calculate a prediction for r_0 as a function of SFR by weighting the fit relation with the stellar mass distribution of each SFR-selected sample. Because $\xi(r)$ is actually a pair-weighted statistic, this method is only an approximation to the r_0 that would be measured from a given stellar mass distribution. The ratio of the mea-

sured r_0 to the predicted r_0 as a function of SFR is shown in Figure 19. If the large-scale clustering amplitude observed can be predicted given the stellar mass distribution of each SFR sample and the observed relation between r_0 and stellar mass, $r_0(\psi)_{\mathrm{obs}}/r_0(\psi)_{\mathrm{fit}}$ would equal one. We find that the mean $r_0(\psi)_{\mathrm{obs}}/r_0(\psi)_{\mathrm{fit}}$ over all SFR is 1.057±0.025; the deviation from unity has a p-value of $p = 0.076$ and therefore is significant at the $p < 0.1$ level. We also find that there is a trend towards larger deviations from the mass-predicted r_0 at higher SFRs, suggesting that most, but not all, of the SFR - r_0 relationship can be explained by the relationship between SFR and stellar mass.

While most of the clustering amplitude as a function of SFR may be explained by the r_0-M_* relation, it is interesting to investigate the SFR-dependent clustering behavior where the stellar mass distributions of SFR-selected samples are equal. In Figure 20, we plot SFR versus stellar mass for our parent DEEP2 sample with contours showing lines of constant $\log(\psi/M_*)$. As we find that r_0 increases with decreasing sSFR (see Figure 12), the clustering amplitude increases from the upper left (high sSFR) to the lower right (low sSFR) in this space. To test whether high SFR galaxies are more clustered than low SFR galaxies with similar stellar masses, we construct a galaxy sample limited in stellar mass to $10<\log(M_*/M_\odot)<11$ and sSFR to $\log(\psi/M_*)<-9.9$, which is complete in the volume between $0.74<z<1.05$. This sample selection is shown with a dotted line in Figure 20. We then perform a linear fit to the SFR-M_* dependence within this selected sample, weighting by the average errors of 0.3 dex in M_* and 0.25 dex in SFR. The resulting fit (shown with a solid black line) roughly corresponds to the location of the star-forming "main sequence" ((MS) e.g., Noeske et al. 2007a) for the selected sample. Separating the galaxy sample into populations above and below the MS, we find that the mean stellar mass is $\log(M_*/M_\odot)=10.36$ for both populations, while the average SFRs are $\log(\psi)=1.24$ $M_\odot$ yr^{-1} and $\log(\psi)=0.84$ $M_\odot$ yr^{-1}, respectively. Comparing their clustering properties, we find galaxies above the MS have a clustering amplitude of $r_0=3.73±0.18$, while galaxies below the MS have $r_0=4.36±0.21$ and are therefore more clustered at a given stellar mass. This confirms that the r_0-sSFR results found above are likely not driven by stellar mass differences between the samples.

While the stellar mass and SFR values used in this study are not necessarily highly accurate on an individual galaxy basis, they do represent the global average well. Any scatter in these values would wash out the observed SFR-M_* relation and clustering correlations in this space. In particular, because the highest SFR galaxies have the bluest restframe colors at a given IR luminosity, it is possible that our color-based stellar masses underestimate the true stellar mass as measured in the IR (Weiner et al., in preparation). We have compared our color-M/L stellar masses to galaxies with measured K-band stellar masses both above and below the MS and find no statistically significant bias in the mass distributions.

The clustering dependence with SFR at a given stellar mass is particularly interesting in light of the differences in galaxy properties observed for galaxies above and be-
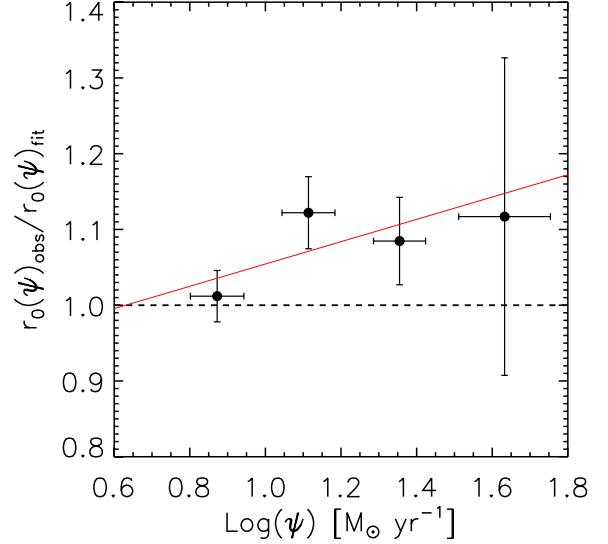

Fig. 19.— The measured clustering scale length $(r_0(\psi)_{\mathrm{obs}})$ for blue galaxy SFR samples normalized to the scale length predicted by the correlation between r_0 and stellar mass. The predicted scale length $(r_0(\psi)_{\mathrm{fit}})$ is generated from an exponential fit to the blue galaxy stellar mass samples (Figure 12) and weighted by the stellar mass distribution of each SFR-selected sample. The weighted mean over all SFRs is $r_0(\psi)_{\mathrm{obs}}/r_0(\psi)_{\mathrm{fit}}=1.057±0.025$, and a weighted linear fit (red, solid line) shows a trend for larger deviation from the stellar mass-predicted r_0 at higher SFR.

low the MS. In general, galaxies above the MS are found to have higher star-forming surface densities, smaller sizes, more dust attenuation, and somewhat higher Sersic indices than galaxies on or below the MS (Schiminovich et al. 2007; Elbaz et al. 2011; Wuyts et al. 2011). In particular, both Elbaz et al. and Wuyts et al. interpret their results to support major mergers as a dominant mechanism of star formation quenching, where galaxies on the MS experience a merger event or some other instability, which leads to a central starburst and bulge formation, and eventually results in a quiescent elliptical galaxy. In this picture, an individual galaxy would move from first being on the MS to being above the MS during the merger stage and then eventually move below the MS as the galaxy becomes quiescent (blue arrows in Figure 20).

However, the clustering results presented here do not support this general picture, as galaxies above the MS are *less* clustered than those on or below the MS. Therefore the majority of the galaxy population above the MS (i.e. with a higher sSFR) can not have previously been on the MS, as the clustering amplitude can not decrease with time. Our clustering results instead support a picture in which most galaxies initially lie above the MS, where they have higher SFRs at a given stellar mass due to internal (non-interacting) processes, and undergo secular evolution down onto and eventually below the MS as their star formation is quenched. While major merger events can certainly occur, their contribution to the overall clustering trends in field galaxies must be sub-dominant. The general evolutionary picture must move from the upper left in the SFR-stellar mass plane down to the lower right to match our clustering measurements. The clustering properties as a function of restframe optical color in both SDSS (Zehavi et al.
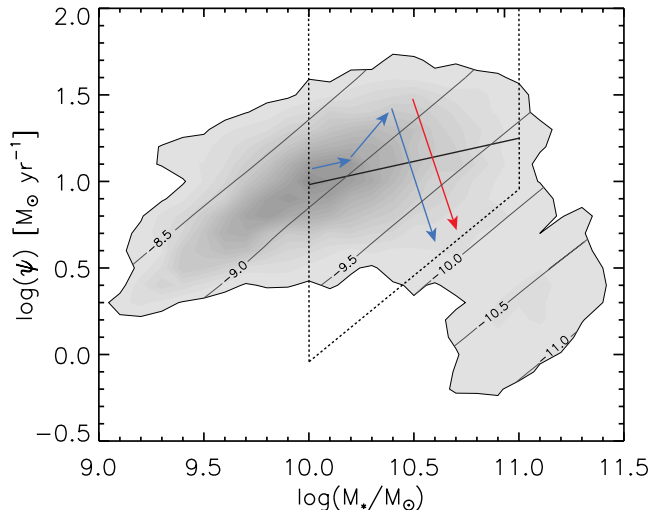
FIG. 20.— The dependence of SFR on stellar mass, overlaid with contours of constant sSFR. Dashed lines show the selection of star-forming galaxies with $z<1.05$ used to measure the clustering of galaxies above and below the star-forming "main sequence". The black solid line shows a linear fit to the SFR-stellar mass relation in this sample. Colored lines show two possible evolution scenarios for star-forming galaxies. The major merger scenario (blue arrows) predicts that galaxies evolve along the star-forming main sequence and undergo a merger event that initially boosts the SFR, followed quickly by a period of star formation quenching and progression onto the red sequence. The secular evolution scenario (red arrows) assumes that galaxies initially lie above the main sequence, during a period of intrinsically rapid star formation and are eventually quenched through internal or secular processes, moving through the main sequence in the process. We find that galaxies above the main sequence have a lower clustering amplitude than galaxies below the main sequence at a given stellar mass. As the clustering of individual galaxies increases with time, our measurements favor the secular evolution scenario, as the galaxy population above the main sequence can not be dominated by galaxies that previously had a lower SFR at a given stellar mass, which are more clustered.

2011) and DEEP2 (C08) also support this scenario, as restframe optical color is well correlated with sSFR at $z \sim 0.1$ and $z \sim 1$, and both studies find that within the star-forming population, bluer galaxies are less clustered than redder galaxies. However, the results presented here do not probe additional evolutionary scenarios whereby the large-scale environment or minor merger events may play a role in galaxy quenching.

6.3. Comparison with Environment Studies

An alternate way to study the dependence of galaxy properties on large-scale structure is through overdensity measurements of a galaxy sample relative to the mean density of galaxies at the same redshift. Such studies measure how a particular galaxy property is correlated with environment and are inherently limited to probe physical scales larger than the density-defining population. At $z \sim 1$, a limiting scale of $\gtrsim 1\ h^{-1}$ Mpc is common. Several environment studies at $z \sim 1$ have found a strong correlation between stellar mass and density, in that galaxies in higher density environments tend to have higher stellar mass (Kauffmann et al. 2004; Cucciati et al. 2006; Cooper et al. 2006; Peng et al. 2010; Sobral et al. 2010). Our results are in broad agreement with these studies, as we find higher clustering amplitudes within increasing stellar mass between $9.6 < \log(M_*/M_\odot) < 11.0$, above which the clustering amplitude remains constant.

There has been some disagreement in the literature, however, as to whether the color-density relationship evolves as a function of redshift. Several previous studies of galaxy environments at $z \sim 1$ have failed to detect any statistically significant relationship between color and density, in contrast to studies at lower redshifts (Cucciati et al. 2006; Scodeggio et al. 2009; Grützbauch et al. 2011). On the other hand, Cooper et al. (2010) probed the most massive DEEP2 galaxies and found a statistically-significant correlation between color and galaxy overdensity, with high mass red galaxies found preferentially in the most dense environments at $z \sim 1$. Cooper et al. emphasizes that while no significant trend in the color-density relation may be *detected* in several environment studies, it is possible that a color-density correlation may simply be missed due to larger statistical errors and/or observational systematics at higher redshifts (e.g due to low sample completeness in VVDS at $z>1$). In our analysis, we do not detect a difference between the clustering of red and blue galaxies at an equivalent stellar mass. However, our samples are defined to probe the bulk color-density relationship at $z \sim 1$, and we do not probe the most over- or under-dense regions specifically, which was a primary focus of Cooper et al. (2010). Our results are consistent with Cooper et al. (2010) in that the color-density trend for high-mass galaxies at $z \sim 1$ is weaker than the stellar mass-density trend; the typical densities of red and blue galaxies at a given stellar mass are not significantly different.

Other environment studies have measured the SFR-density relationship as a function of redshift and stellar mass. Locally, this relation is monotonic, with lower-SFR galaxies found in higher density environments Gómez et al. (2003). At earlier times, the SFR-density relationship was quite different; dense environments are associated with both low and high SFRs (Elbaz et al. 2007, CP08, Sobral et al. 2010). Our SFR-clustering results at $z \sim 1$ are in broad agreement with these studies, with the highest-SFR blue galaxies having roughly the same clustering strength as the lowest-SFR red galaxies. The similar environments found for galaxy populations with vastly different SFRs ($\log(\psi) < 0.5\ M_\odot\ {\rm yr}^{-1}$ and $\log(\psi) > 1.5\ M_\odot\ {\rm yr}^{-1}$) indicate that the processes leading to the large-scale clustering and quenching of star formation in massive galaxies are primarily independent. One possible scenario is that rapidly star-forming blue galaxies at these redshifts are progenitors of the quiescent red galaxies found at later epochs (Cooper et al. 2006, C08). The preponderance of quiescent galaxies found in high density regions at $z \sim 1$ and the relative paucity of high SFR blue galaxies at low redshifts gives the appearance that the large-scale environment and quenching are related.

Mechanisms proposed to explain the evolution of the observed SFR-density relation involve the quenching of star formation in a variety of isolated and merging systems (Sobral et al. 2010; Peng et al. 2010) and include effects such as virial heating of cold gas needed for star formation and the rate of gas exhaustion. However, as pointed out in the previous section, it seems likely that quenching specifically from major mergers plays a sub-dominant role at $z \sim 1$; the clustering of star-forming galaxies at a fixed stellar mass increases monotonically

with decreasing SFR, not vice-versa. Our results support the theory that a simple sSFR-M_* relation, such as proposed "mass-quenching" models where the quenching rate for galaxies at or above M^* is proportional to their stellar mass (Noeske et al. 2007b; Peng et al. 2010), should reproduce the gross relationship between star-formation, stellar mass, and clustering on large scales. However, we caution that not *all* quenching in star-forming galaxies must follow this form, as our samples probe only the average clustering properties of the $z \sim 1$ galaxy distribution.

6.4. *Small-scale Clustering Behavior*

We now turn to our clustering results on small scales, below $r_p \sim 1$ h^{-1} Mpc. In Section 5.1, we found that $\xi(r_p, \pi)$ for blue galaxies selected by stellar mass exhibits stronger "Fingers of God" on small scales at higher stellar mass (see Figure 8), indicating that higher-stellar mass blue galaxies reside in halos with higher velocity dispersions and therefore likely reside in higher mass halos than lower-stellar mass blue galaxies. Such an obvious increase in the "Fingers of God" within $\xi(r_p, \pi)$ is not seen for blue galaxy samples selected by SFR or sSFR, suggesting that these properties do not correlate with the dark matter halo mass as directly as stellar mass does. Although we do not show them here, we find that all red galaxy samples exhibit strong "Fingers of God", independent of the stellar mass or SFR and similar to the red luminosity samples in C08 (see their Figure 8).

In order to reveal any relative change in the small-scale clustering amplitude, we divide $\omega_p(r_p)$ on all scales by the best fit power law on scales 1-10 h^{-1} Mpc and look for excess clustering below $r_p \leq 0.3$ h^{-1} Mpc relative to this best fit power law. In HOD models, the slope of $\omega_p(r_p)$ on these small scales, where the one-halo term dominates the correlation function, is governed by the relative number of central and satellite galaxy pairs within an individual halo, as well as the location of the probed halo mass scale on the halo mass function (Berlind & Weinberg 2002; Zehavi et al. 2005; Zheng et al. 2005; Skibba & Sheth 2009). For massive galaxy samples with a minimum halo mass corresponding to $\gtrsim 10^{12.5}$ $h^{-1}M_\odot$ at $z = 1$, the $\omega_p(r_p)$ amplitude rapidly increases on small scales due to a greater contribution from central-satellite and satellite-satellite pairs (Sheth & Tormen (2002); Tinker et al. (2008); see also Appendix A of Zheng et al. (2009) for further details). Such massive halos are near the exponential tail of the halo mass function, and higher-mass halos are increasingly rare in the volume surveyed by DEEP2.

For our galaxy samples defined by stellar mass, we find no significant increase in clustering on small scales for any of the blue galaxy samples. However, both mass-selected red galaxy samples exhibit enhanced clustering on scales below $r_p \leq 0.3$ h^{-1} Mpc ($p = 0.005$ for $10.5 < \log(M_*/M_\odot) < 11.0$ and $p = 0.04$ for $\log(M_*/M_\odot) > 11.0$). This difference between blue and red galaxy mass samples may reflect a higher contribution from central-satellite pairs, due to both a lower satellite fraction for massive red galaxies (compared to blue galaxies) and the higher minimum halo mass ($\sim 10^{12.5} h^{-1} M_\odot$), as discussed above. The lack of a detectable small-scale rise for the blue galaxy sample at an equivalent stellar mass may be due in part to larger measurement errors in the highest mass sample (see the right panel of Figure 11) and/or a larger contribution from satellite-satellite pairs than central-satellite pairs, which smoothes the transition in $\omega_p(r_p)$ between the one-halo to two-halo terms. The small-scale clustering in color-independent stellar mass samples is driven primarily by the fraction of red to blue galaxies at a fixed stellar mass. Accordingly, we observe that the color-independent samples exhibit a similar small-scale rise at high stellar mass due to the high fraction of red galaxies present in the sample.

When binned by SFR, we find that red galaxies with low SFRs do not show a rise on small scales, while blue galaxies do exhibit a 7-fold increase in small-scale clustering amplitude over the best-fit large-scale power law below $r_p \leq 0.3$ h^{-1} Mpc. While the $\omega_p(r_p)$ error in the highest-SFR blue galaxy sample ($\log(\psi) > 1.5$ $M_\odot$ yr^{-1}) is the largest of all measured blue galaxy samples, the deviation from the large-scale power law has a p value of $p = 0.038$ and is statistically significant at the $p < 0.05$ level. One possible explanation for the correlation between high SFR and increased small-scale clustering amplitude is that star formation is being triggered by galaxy interactions, either through merger events or tidal interactions (e.g. Barton et al. 2007). Late-type galaxies in the blue cloud contain large gas reservoirs which can support enhanced levels of star formation triggered though close interactions of galaxy pairs. Enhanced IR luminosity, which is tightly correlated with star formation, has been previously observed in extremely blue DEEP2 galaxies in close kinematic galaxy pairs ($\delta r_p = 50$ h^{-1} kpc) within the EGS (Lin et al. 2007). Further, Robaina et al. (2009) show enhanced clustering with SFR on slightly larger scales ($40 < r_p < 180$ h^{-1} kpc) between $0.4 < z < 0.8$ in a sample of COMBO-17 galaxies (Wolf et al. 2003) matched to *Spitzer* 24μm measurements.

Our results show a similar increase in small-scale clustering power at high SFR, on scales $r_p \leq 0.3$ h^{-1} Mpc. However, we have demonstrated that an increased SFR is also correlated with higher stellar mass, and therefore it is also possible that galaxies with higher stellar mass have a stronger one-halo term due to their higher halo mass. It is possible that both stellar mass and SFR enhancement are correlated with the increase clustering seen on small-scales in SFR-selected blue galaxies. We note, however, that red galaxies with low SFR have similar halo masses to the high-SFR blue galaxies and do not show a similar rise, indicating that SFR enhancement is likely more strongly correlated with the increased clustering signal.

These small-scale clustering trends allow us to interpret the behavior seen as a function of luminosity in C08 (their Figure 10), who detected a relative small-scale rise for the brightest blue galaxies and a marginal increase for bright red galaxies. Figure 2 shows that blue galaxies with the highest SFRs also have the highest luminosities, and therefore the observed small-scale rise for bright blue galaxies may have been due in part to both higher stellar masses and SFR enhancement. The small-scale rise observed here for massive red galaxies is likely reflected in the marginally-significant increase seen for bright red galaxies in C08. As the mass-to-light ratio varies across

the red sequence, a given luminosity range corresponds to a wider range in stellar mass; if stellar mass is more strongly linked to halo mass, luminosity-selected samples will have a broader host mass range and hence exhibit a weaker small-scale clustering signal.

Turning to sSFR, we find that galaxies that are forming stars most rapidly relative to their existing stellar mass have an increased clustering amplitude on small scales. Interestingly, *both* the high-sSFR sub-samples of the blue and red galaxy population show a small-scale rise at $r_p \leq 0.3$ h^{-1} Mpc. In each sample, we measure a 4-fold increase in $\omega_p(r_p)$ relative to the large-scale power law fit over r_p=1-10 h^{-1} Mpc scales. The increase in clustering is significant at the $p < 0.05$ level in both galaxy samples. Unlike the previous small-scale clustering results with SFR, the sSFR samples have normalized the SFR relative to the stellar mass, and therefore the measured small-scale rise will be more directly connected to enhanced star formation at a fixed stellar mass. Because sSFR is highly correlated with star formation history and restframe color, the galaxies demonstrating this increased small-scale clustering are the bluest members of their respective populations (e.g. the bluest blue galaxies and the bluest red galaxies).

Li et al. (2008) measured the clustering of SDSS galaxies selected by sSFR and found enhanced small-scale galaxy clustering in the local Universe, with >40% of these galaxies having close (r_p <100 kpc) companions. They conclude that the observed clustering behavior is a signature of tidal interactions between galaxy pairs inside the same dark matter halo, which leads to an inflow of cold gas and enhanced star formation. Evidence for enhanced sSFR on small scales was also measured from close pairs of blue galaxies (r_p<50 h^{-1} kpc) at higher redshift in PRIMUS between 0.25<z<0.5 (Wong et al. 2011) and in DEEP2 between 0.1<z<1.1 (Lin et al. 2007). Robaina et al. (2009) also found enhanced clustering on scales r_p<40 kpc for star-forming galaxies with $M_* > 10^{10}$ $M_\odot$ between 0.4<z<0.8. While we define "small-scales" at a larger scale threshold of $r_p \leq 0.3$ h^{-1} Mpc, we also find statistically significant evidence for enhanced small-scale clustering with sSFR. These results support our interpretation that enhanced star formation, possibly triggered from galaxy tidal interactions, is correlated with the observed small-scale rise in our blue galaxy sample with high sSFR.

However, enhanced small-scale clustering for high-sSFR red galaxies may be somewhat surprising. The range of sSFR for which we find this enhancement ($-10 < \log(\psi/M_*) < -11$) is often referred to as the "green valley", a transition region from blue star-forming galaxies to red quiescent galaxies (Martin et al. 2007; Salim et al. 2009; Mendez et al. 2011). The enhanced clustering could be due to recent merger events or tidal disruptions between red and blue galaxy pairs where the blue galaxy has provided additional gas for star formation in the quiescent galaxy. Robaina et al. (2009) found that major interactions can contribute significantly to the small-scale clustering amplitude for the most dust-obscured starbursts, which may be selected in our DEEP2 sample as red with the restframe color cut of Equation 1. Alternatively, close interactions between blue galaxy pairs could temporarily boost the SFR and eventually lead to quenching, which would move galaxies from the blue cloud to the red sequence. As we argued in the last subsection, however, such events must be sub-dominant to the general quenching trend in individual halos.

7. CONCLUSIONS

In this study, we measure the two-point correlation function of complete DEEP2 galaxy samples selected by stellar mass, SFR and sSFR and separated by restframe color. We fit a power law to the projected correlation function and measure the bias and clustering scale length and slope on scales of 1-10 h^{-1} Mpc ($\bar{r}_p$=4.1 h^{-1} Mpc), where the two-halo term dominates the 2PCF. We also study the relative shape of the correlation function on small and large scales, which depends on the satellite fraction and dark matter halo mass. We summarize our findings as follows:

1. The large-scale galaxy clustering amplitude increases monotonically as a function of stellar mass for star-forming galaxies with $9.6 < \log(M_*/M_\odot) < 11$, indicating that stellar mass closely tracks halo mass at $z \sim 1$. Within the limited mass range probed for red galaxies ($10.5 < \log(M_*/M_\odot) < 11.5$), we find no significant trend between stellar mass and clustering amplitude. Within the measurement errors, our results agree with a $z \sim 1$ clustering analysis from VVDS (Meneux et al. 2008) in the stellar mass range where both DEEP2 and VVDS samples are complete.

2. Within the blue, star-forming galaxy population, the large-scale clustering amplitude increases as a function of increasing SFR. Red galaxies with low SFRs are strongly clustered and show no dependence on SFR within the range probed. We find the highest-SFR blue galaxies have the same clustering amplitude as red galaxies, as seen in previous DEEP2 environment studies.

3. The observed trend between large-scale clustering amplitude and SFR can primarily be accounted for by the observed correlation between clustering amplitude and stellar mass. However, the r_0-stellar mass relation alone does not fully predict the clustering amplitude at all SFRs; there is a small clustering excess at high SFR above what is predicted by the stellar mass of each sample alone. This suggests that most, but not all, of the correlation between large-scale clustering amplitude and SFR can be attributed to the SFR-stellar mass relation.

4. Galaxy samples selected by sSFR show similar large-scale clustering trends as samples selected by stellar mass. The clustering amplitude decreases with increasing sSFR (corresponding to bluer restframe color) while red galaxies with low sSFRs have a constant clustering strength in the range probed. While the large-scale clustering amplitude only mildly depends on sSFR for $-11.0 < \log(\psi/M_*) < -9.5$, r_0 drops significantly between $-9.5 < \log(\psi/M_*) < -8.5$, similar to the trend observed locally in SDSS.

5. By constructing stellar mass-limited star-forming galaxy samples above and below the SFR-stellar mass "main sequence", we find that the clustering amplitude increases with decreasing SFR at a fixed stellar mass (i.e. below the main sequence), which confirms that the clustering trends seen with sSFR are not driven entirely by stellar mass. Given that galaxies below the main sequence are more clustered than those above, the bulk of the population above the main sequence can not be dominated by galaxies that used to be on the main sequence and are currently undergoing major merger events. Instead, galaxies must smoothly evolve from above the main sequence to below it, as the clustering of galaxies can only increase with time.

6. We detect enhanced clustering on scales less than $r_p \leq 0.3\ h^{-1}$ Mpc, relative to larger scales, for high stellar mass red galaxies, high SFR blue galaxies, and the highest sSFR sub-samples of both red and blue galaxy populations. The increased small-scale clustering may reflect a combination of effects, including a changing satellite fraction, higher halo mass, and/or enhanced SFR. We conclude that triggered star formation due to close galaxy interactions is a likely explanation for the enhanced clustering seen at high sSFR.

As our analysis uses the two-point correlation function formalism and measures clustering properties for several important galaxy properties, we expect these results to be highly useful for galaxy evolution models. In particular, HOD and abundance matching models should greatly benefit from measurements of the clustering amplitude at $z \sim 1$ with respect to stellar mass, SFR, and sSFR. We also anticipate that the bias values calculated here as a function of stellar mass and SFR will be used in projections of future BAO surveys that will probe the $z>1$ universe.

REFERENCES

Abazajian, K. N., Adelman-McCarthy, J. K., Agüeros, M. A., et al. 2009, ApJS, 182, 543
Barton, E. J., Arnold, J. A., Zentner, A. R., Bullock, J. S., & Wechsler, R. H. 2007, ApJ, 671, 1538
Borch, A., Meisenheimer, K., Bell, E. F., et al. 2006, A&A, 453, 869
Behroozi, P. S., Conroy, C., & Wechsler, R. H. 2010, ApJ, 717, 379
Bell, E. F., McIntosh, D. H., Katz, N., & Weinberg, M. D. 2003, ApJS, 149, 289
Benson, A. J., Cole, S., Frenk, C. S., Baugh, C. M., & Lacey, C. G. 2000, MNRAS, 311, 793
Berlind, A. A., & Weinberg, D. H. 2002, ApJ, 575, 587
Blake, C., Jurek, R. J., Brough, S., et al. 2009, MNRAS, 395, 240
Blanton, M. R. 2006, ApJ, 648, 268
Bundy, K., et al. 2006, ApJ, 651, 120
Capak, P., Aussel, H., Ajiki, M., et al. 2007, ApJS, 172, 99
Coil, A. L., et al. 2008, ApJ, 672, 153
Coil, A. L., Blanton, M. R., Burles, S. M., et al. 2011, ApJ, 741, 8
Colless, M., Dalton, G., Maddox, S., et al. 2001, MNRAS, 328, 1039
Conroy, C., Prada, F., Newman, J. A., et al. 2007, ApJ, 654, 153
Conroy, C., & Wechsler, R. H. 2009, ApJ, 696, 620
Cooper, M. C., et al. 2006, MNRAS, 370, 198
Cooper, M. C., Newman, J. A., Weiner, B. J., et al. 2008, MNRAS, 383, 1058
Cooper, M. C., Coil, A. L., Gerke, B. F., et al. 2010, MNRAS, 409, 337
Cooray, A., & Sheth, R. 2002, Phys. Rep., 372, 1
Coupon, J., Kilbinger, M., McCracken, H. J., et al. 2012, A&A, 542, A5
Cowie, L. L., Songaila, A., Hu, E. M., & Cohen, J. G. 1996, AJ, 112, 839
Cucciati, O., Iovino, A., Marinoni, C., et al. 2006, A&A, 458, 39
Davis, M., & Peebles, P. J. E. 1983, ApJ, 267, 465
Davis, M., et al. 2007, ApJ, 660, L1

Eisenstein, D. J., Zehavi, I., Hogg, D. W., et al. 2005, ApJ, 633, 560
Eisenstein, D. J., Weinberg, D. H., Agol, E., et al. 2011, AJ, 142, 72
Elbaz, D., Daddi, E., Le Borgne, D., et al. 2007, A&A, 468, 33
Elbaz, D., Dickinson, M., Hwang, H. S., et al. 2011, A&A, 533, A119
Faber, S. M., Phillips, A. C., Kibrick, R. I., et al. 2003, Proc. SPIE, 4841, 1657
Felten, J. E. 1976, ApJ, 207, 700
Gehrels, N. 1986, ApJ, 303, 336
Gerke, B. F., et al. 2007, MNRAS, 376, 1425
Giavalisco, M., Ferguson, H. C., Koekemoer, A. M., et al. 2004, ApJ, 600, L93
Gómez, P. L., Nichol, R. C., Miller, C. J., et al. 2003, ApJ, 584, 210
Grützbauch, R., Conselice, C. J., Varela, J., et al. 2011, MNRAS, 411, 929
Hogg, D. W. 1999, arXiv:astro-ph/9905116
Hopkins, A. M., & Beacom, J. F. 2006, ApJ, 651, 142
Ilbert, O., Capak, P., Salvato, M., et al. 2009, ApJ, 690, 1236
Jenkins, A., Frenk, C. S., White, S. D. M., et al. 2001, MNRAS, 321, 372
Jing, Y. P. 1998, ApJ, 503, L9
Kaiser, N. 1984, ApJ, 284, L9
Kaiser, N. 1987, MNRAS, 227, 1
Kauffmann, G., White, S. D. M., Heckman, T. M., et al. 2004, MNRAS, 353, 713
Kennicutt, R. C., Jr. 1998, ARA&A, 36, 189
Kravtsov, A. V., Berlind, A. A., Wechsler, R. H., et al. 2004, ApJ, 609, 35
Landy, S. D., & Szalay, A. S. 1993, ApJ, 412, 64
Leauthaud, A., Tinker, J., Bundy, K., et al. 2012, ApJ, 744, 159
Le Fevre, O., Vettolani, G., Maccagni, D., et al. 2003, Proc. SPIE, 4834, 173
Li, C., Kauffmann, G., Jing, Y. P., et al. 2006, MNRAS, 368, 21

Li, C., Kauffmann, G., Heckman, T. M., Jing, Y. P., & White, S. D. M. 2008, MNRAS, 385, 1903

Lin, L., Koo, D. C., Weiner, B. J., et al. 2007, ApJ, 660, L51

Lin, L., Dickinson, M., Jian, H.-Y., et al. 2012, ApJ, 756, 71

Lilly, S. J., Le Fèvre, O., Renzini, A., et al. 2007, ApJS, 172, 70

Martin, D. C., Wyder, T. K., Schiminovich, D., et al. 2007, ApJS, 173, 342

Mendez, A. J., Coil, A. L., Lotz, J., et al. 2011, ApJ, 736, 110

Meneux, B., Guzzo, L., Garilli, B., et al. 2008, A&A, 478, 299

Mo, H. J., & White, S. D. M. 1996, MNRAS, 282, 347

Mostek, N., Coil, A. L., Moustakas, J., Salim, S., & Weiner, B. J. 2012, ApJ, 746, 124

Mostek, N., Barbary, K., Bebek, C. J., Dey, A. 2012, Proc. SPIE, 8446, 24

Moster, B. P., Somerville, R. S., Maulbetsch, C., et al. 2010, ApJ, 710, 903

Moustakas, J., Kennicutt, Jr., R. C. & Tremonti, C. A. 2006, ApJ, 642, 775.

Muldrew, S. I., Croton, D. J., Skibba, R. A., et al. 2012, MNRAS, 419, 2670

Newman, J. A., & Davis, M. 2002, ApJ, 564, 567

Newman, J. A., Cooper, M. C., Davis, M., et al. 2012, ApJS, submitted (arXiv:1203.3192)

Noeske, K. G., et al. 2007, ApJ, 660, L43

Noeske, K. G., et al. 2007, ApJ, 660, L47

Peacock, J. A., & Smith, R. E. 2000, MNRAS, 318, 1144

Peacock, J. A., Cole, S., Norberg, P., et al. 2001, Nature, 410, 169

Peng, Y.-j., Lilly, S. J., Kovač, K., et al. 2010, ApJ, 721, 193

Robaina, A. R., Bell, E. F., Skelton, R. E., et al. 2009, ApJ, 704, 324

Salim, S., et al. 2009, ApJ, 700, 161

Salpeter, E. E. 1955, ApJ, 121, 161

Scodeggio, M., Vergani, D., Cucciati, O., et al. 2009, A&A, 501, 21

Scoville, N., Aussel, H., Brusa, M., et al. 2007, ApJS, 172, 1

Seljak, U. 2000, MNRAS, 318, 203

Seljak, U., & Warren, M. S. 2004, MNRAS, 355, 129

Schiminovich, D., Wyder, T. K., Martin, D. C., et al. 2007, ApJS, 173, 315

Schlegel, D., Abdalla, F., Abraham, T., et al. 2011, arXiv:1106.1706

Sheth, R. K., & Tormen, G. 1999, MNRAS, 308, 119

Sheth, R. K., Mo, H. J., & Tormen, G. 2001, MNRAS, 323, 1

Sheth, R. K., & Tormen, G. 2002, MNRAS, 329, 61

Skibba, R. A., & Sheth, R. K. 2009, MNRAS, 392, 1080

Smith, R. E., Peacock, J. A., Jenkins, A., et al. 2003, MNRAS, 341, 1311

Sobral, D., Best, P. N., Geach, J. E., et al. 2010, MNRAS, 404, 1551

Tinker, J., Kravtsov, A. V., Klypin, A., et al. 2008, ApJ, 688, 709

van Dokkum, P. G., Labbé, I., Marchesini, D., et al. 2009, PASP, 121, 2

Wake, D. A., Whitaker, K. E., Labbé, I., et al. 2011, ApJ, 728, 46

Weiner, B. J., et al. 2009, ApJ, 692, 187

Willmer, C. N. A., et al. 2006, ApJ, 647, 853

Wolf, C., Meisenheimer, K., Rix, H.-W., et al. 2003, A&A, 401, 73

Wong, K. C., Blanton, M. R., Burles, S. M., et al. 2011, ApJ, 728, 119

Wuyts, S., Förster Schreiber, N. M., van der Wel, A., et al. 2011, ApJ, 742, 96

Yan, R., White, M., & Coil, A. L. 2004, ApJ, 607, 739

Yan, R., Newman, J. A., Faber, S. M., Konidaris, N., Koo, D., & Davis, M. 2006, ApJ, 648, 281

York, D. G., Adelman, J., Anderson, J. E., Jr., et al. 2000, AJ, 120, 1579

Zehavi, I., Zheng, Z., Weinberg, D. H., et al. 2005, ApJ, 630, 1

Zehavi, I., Zheng, Z., Weinberg, D. H., et al. 2011, ApJ, 736, 59

Zehavi, I., Patiri, S., & Zheng, Z. 2012, ApJ, 746, 145

Zheng, Z., Berlind, A. A., Weinberg, D. H., et al. 2005, ApJ, 633, 791

Zheng, Z., Coil, A. L., & Zehavi, I. 2007, ApJ, 667, 760

Zheng, Z., Zehavi, I., Eisenstein, D. J., Weinberg, D. H., & Jing, Y. P. 2009, ApJ, 707, 554

Zheng, Z., Zehavi, I., Eisenstein, D. J., Weinberg, D. H., & Jinp, Y. P. 2009, ApJ, 707, 554

Zhu, G., Moustakas, J. & Blanton, M. R. 2009, ApJ, 701, 86.

Zhu, G., Blanton, M. R., Burles, S. M., et al. 2011, ApJ, 726, 110

TABLE 1
RESULTS FOR STELLAR MASS THRESHOLD SAMPLES

Color	M_*	$<M_*>$	N_{gal}	n	$\sigma_{\rm cv}$	z Range	$<z>$	r_0	γ	Bias	$M_{\rm min}$	$<M_{\rm halo}>$
	[$\log(M_\odot)$]			[$10^{-4}\ h^3$ Mpc^{-3}]				[h^{-1} Mpc]			[$\log(h^{-1}M_\odot)$]	
All	>10.5	10.90	4201	16.9 ± 0.7	8.2	0.74–1.05	0.89	4.99 ± 0.14	1.78 ± 0.12	1.77 ± 0.06	12.48	12.95
All	>10.8	11.08	2400	11.4 ± 0.5	4.7	0.74–1.05	0.89	5.33 ± 0.16	1.88 ± 0.14	1.87 ± 0.06	12.61	13.05
Blue	>9.6	10.18	9885	23.0 ± 1.7	7.2	0.74–1.05	0.89	3.46 ± 0.12	1.59 ± 0.06	1.35 ± 0.05	11.67	12.32
Blue	>9.9	10.33	7268	29.4 ± 1.0	8.5	0.74–1.05	0.90	3.66 ± 0.14	1.53 ± 0.08	1.42 ± 0.07	11.85	12.47
Blue	>10.2	10.51	4331	21.0 ± 0.6	8.2	0.74–1.05	0.91	4.13 ± 0.14	1.61 ± 0.08	1.50 ± 0.06	12.03	12.60
Blue	>10.5	10.73	1969	9.9 ± 0.4	3.8	0.74–1.05	0.91	4.29 ± 0.34	1.60 ± 0.10	1.60 ± 0.10	12.22	12.75
Blue	>9.9	10.34	12613	14.0 ± 0.9	3.2	0.74–1.40	1.03	3.78 ± 0.10	1.60 ± 0.06	1.50 ± 0.05	12.03	12.60
Blue	>10.2	10.51	7844	12.5 ± 0.5	4.1	0.74–1.40	1.04	4.24 ± 0.09	1.77 ± 0.07	1.59 ± 0.04	12.20	12.74
Blue	>10.5	10.73	3567	6.7 ± 0.3	2.0	0.74–1.40	1.04	4.40 ± 0.18	1.73 ± 0.15	1.71 ± 0.08	12.40	12.89
Blue	>10.8	10.97	1134	2.3 ± 0.1	0.9	0.74–1.40	1.04	5.89 ± 0.50	1.63 ± 0.38	2.11 ± 0.13	12.87	13.26
Red	>10.5	11.04	2232	8.5 ± 0.6	4.4	0.74–1.05	0.88	5.28 ± 0.26	1.98 ± 0.19	1.84 ± 0.05	12.57	13.02
Red	>11.0	11.23	1200	5.8 ± 0.3	3.2	0.74–1.05	0.89	4.96 ± 0.24	1.72 ± 0.16	1.81 ± 0.08	12.53	12.99

TABLE 2
RESULTS FOR STELLAR MASS BIN SAMPLES

Color	M_*	$<M_*>$	N_{gal}	n	$\sigma_{\rm cv}$	z Range	$<z>$	r_0	γ	Bias
	[$\log(M_\odot)$]			[$10^{-4}\ h^3$ Mpc^{-3}]				[h^{-1} Mpc]		
All	10.4–10.8	10.59	2554	–	–	0.74–1.05	0.90	4.52 ± 0.21	1.70 ± 0.15	1.60 ± 0.05
All	>10.8	11.08	2400	11.4 ± 0.5	4.7	0.74–1.05	0.89	5.33 ± 0.16	1.88 ± 0.14	1.87 ± 0.06
Blue	9.6–10.0	9.81	3573	7.0 ± 1.5	2.9	0.74–1.05	0.86	3.02 ± 0.18	1.65 ± 0.14	1.18 ± 0.06
Blue	10.0–10.4	10.19	3643	14.9 ± 0.7	3.8	0.74–1.05	0.90	3.37 ± 0.14	1.55 ± 0.12	1.34 ± 0.07
Blue	>10.4	10.65	2676	13.4 ± 0.5	5.2	0.74–1.05	0.91	4.50 ± 0.17	1.68 ± 0.11	1.62 ± 0.08
Blue	9.9–10.2	10.05	4774	4.7 ± 0.7	1.7	0.74–1.40	1.02	2.80 ± 0.41	1.30 ± 0.16	1.35 ± 0.10
Blue	10.2–10.5	10.34	4279	6.4 ± 0.4	2.0	0.74–1.40	1.04	3.71 ± 0.21	1.76 ± 0.09	1.48 ± 0.07
Blue	10.5–10.8	10.63	2435	4.4 ± 0.2	1.5	0.74–1.40	1.04	4.14 ± 0.21	1.90 ± 0.19	1.57 ± 0.09
Blue	>10.8	10.97	1134	2.6 ± 0.1	0.9	0.74–1.40	1.04	5.89 ± 0.50	1.63 ± 0.38	2.11 ± 0.13
Red	10.5-11.0	10.81	1034	3.8 ± 0.6	2.0	0.74–1.05	0.87	5.00 ± 0.63	1.65 ± 0.17	1.76 ± 0.14
Red	>11.0	11.23	1200	5.8 ± 0.3	3.2	0.74–1.05	0.89	4.96 ± 0.24	1.72 ± 0.16	1.81 ± 0.08

TABLE 3
RESULTS FOR STAR FORMATION RATE THRESHOLD SAMPLES

Color	SFR	$<$SFR$>$	N_{gal}	n	$\sigma_{\rm cv}$	z Range	$<z>$	r_0	γ	Bias	$M_{\rm min}$	$<M_{\rm halo}>$
	[$\log(M_\odot$ yr^{-1})]			[10^{-4} h^3 Mpc^{-3}]				[h^{-1} Mpc]			[$\log(h^{-1}M_\odot)$]	
Blue	>0.75	1.05	8542	39.4 ± 0.9	8.7	0.74–1.05	0.90	3.46 ± 0.14	1.53 ± 0.04	1.38 ± 0.05	11.75	12.39
Blue	>1.00	1.22	4456	22.2 ± 0.6	5.2	0.74–1.05	0.91	3.70 ± 0.27	1.53 ± 0.17	1.44 ± 0.08	11.90	12.50
Blue	>1.25	1.41	1693	8.2 ± 0.4	1.7	0.74–1.05	0.91	3.80 ± 0.26	1.60 ± 0.22	1.48 ± 0.09	11.99	12.57
Blue	>1.00	1.22	7507	17.8 ± 0.5	5.2	0.74–1.25	1.01	3.90 ± 0.20	1.62 ± 0.08	1.52 ± 0.07	12.24	12.64
Blue	>1.25	1.41	4355	7.3 ± 0.3	3.5	0.74–1.40	1.12	3.99 ± 0.25	1.37 ± 0.13	1.72 ± 0.08	12.41	12.90
Blue	>1.50	1.62	1114	2.3 ± 0.1	0.3	0.74–1.40	1.13	4.45 ± 1.19	1.38 ± 0.27	1.97 ± 0.32	12.64	13.07
Red	>-0.1	0.39	2041	6.4 ± 0.7	2.9	0.74–1.05	0.88	5.28 ± 0.28	1.84 ± 0.24	1.84 ± 0.06	12.58	13.02
Red	>0.4	0.65	954	4.7 ± 0.3	1.7	0.74–1.05	0.90	5.26 ± 0.63	1.65 ± 0.31	1.90 ± 0.13	12.64	13.08

TABLE 4
RESULTS FOR STAR FORMATION RATE BINNED SAMPLES

Color	SFR	$<$SFR$>$	N_{gal}	n	$\sigma_{\rm cv}$	z Range	$<z>$	r_0	γ	Bias
	[$\log(M_\odot$ yr^{-1})]			[10^{-4} h^3 Mpc^{-3}]				[h^{-1} Mpc]		
Blue	0.75–1.00	1.05	4091	17.8 ± 0.7	5.5	0.74–1.05	0.90	3.05 ± 0.13	1.44 ± 0.11	1.31 ± 0.04
Blue	1.00–1.25	1.22	2765	14.0 ± 0.5	3.8	0.74–1.05	0.91	3.61 ± 0.47	1.37 ± 0.18	1.47 ± 0.08
Blue	>1.25	1.41	1693	8.2 ± 0.4	1.7	0.74–1.05	0.91	3.88 ± 0.27	1.53 ± 0.16	1.53 ± 0.10
Blue	1.00–1.25	1.11	4634	12.8 ± 0.4	3.2	0.74–1.25	1.01	3.91 ± 0.27	1.62 ± 0.15	1.48 ± 0.07
Blue	1.25–1.50	1.35	3243	5.2 ± 0.2	3.2	0.74–1.40	1.11	3.93 ± 0.18	1.48 ± 0.22	1.63 ± 0.07
Blue	>1.50	1.62	1114	2.3 ± 0.1	0.4	0.74–1.40	1.13	4.45 ± 1.19	1.38 ± 0.27	1.97 ± 0.32
Red	-0.1–0.4	0.14	1081	2.9 ± 0.6	2.6	0.74–1.05	0.87	5.00 ± 0.29	2.10 ± 0.40	1.72 ± 0.08
Red	>0.4	0.65	954	4.7 ± 0.3	1.7	0.74–1.05	0.90	5.26 ± 0.63	1.65 ± 0.31	1.90 ± 0.13

TABLE 5
RESULTS FOR SPECIFIC STAR FORMATION RATE THRESHOLD SAMPLES

Color	sSFR	$<$sSFR$>$	N_{gal}	n	$\sigma_{\rm cv}$	z Range	$<z>$	r_0	γ	Bias	$M_{\rm min}$	$<M_{\rm halo}>$
	[$\log(\mathrm{yr}^{-1})$]			[10^{-4} h^3 Mpc^{-3}]				[h^{-1} Mpc]			[$\log(h^{-1}M_\odot)$]	
Blue[a]	<-8.60	-9.13	5777	28.9 ± 0.7	8.5	0.74–1.05	0.91	3.97 ± 0.16	1.47 ± 0.08	1.52 ± 0.06	12.07	12.64
Blue	<-8.95	-9.30	3819	19.2 ± 0.5	8.2	0.74–1.05	0.91	4.43 ± 0.20	1.63 ± 0.07	1.59 ± 0.07	12.20	12.74
Blue	<-9.30	-9.54	1651	8.2 ± 0.4	4.7	0.74–1.05	0.91	4.66 ± 0.35	1.66 ± 0.14	1.67 ± 0.09	12.34	12.84
Blue[b]	<-8.60	-8.79	7144	13.1 ± 0.4	3.2	0.74–1.40	1.11	4.21 ± 0.11	1.70 ± 0.07	1.64 ± 0.05	12.29	12.80
Blue	<-8.95	-9.11	4693	9.3 ± 0.3	2.9	0.74–1.40	1.07	4.54 ± 0.10	1.82 ± 0.07	1.70 ± 0.04	12.38	12.88
Blue	<-9.30	-9.54	2013	3.8 ± 0.2	1.5	0.74–1.40	1.03	4.62 ± 0.24	1.84 ± 0.18	1.76 ± 0.08	12.47	12.94
Red[a]	<-9.90	-10.59	1641	8.2 ± 0.4	3.8	0.74–1.05	0.89	5.17 ± 0.23	1.80 ± 0.13	1.84 ± 0.06	12.58	13.02
Red	<-10.6	-10.91	795	4.1 ± 0.3	2.6	0.74–1.05	0.89	5.04 ± 0.32	2.04 ± 0.25	1.81 ± 0.11	12.54	12.99

[a] $z<1.05$ galaxy samples are limited to $M_B<-20.5$.
[b] $z<1.4$ blue galaxy samples are limited to $M_B<-21.0$.

TABLE 6
RESULTS FOR SPECIFIC STAR FORMATION RATE BINNED SAMPLES

Color	sSFR	$<$sSFR$>$	N_{gal}	n	$\sigma_{\rm cv}$	z Range	$<z>$	r_0	γ	Bias
	[log(yr^{-1})]			[10^{-4} h^3 Mpc^{-3}]				[h^{-1} Mpc]		
Blue[a]	-8.60 − -8.95	-8.80	1959	9.6 ± 0.4	3.2	0.74–1.05	0.91	3.64 ± 0.36	1.59 ± 0.09	1.42 ± 0.11
Blue	-8.95 − -9.30	-9.11	2170	11.1 ± 0.4	3.8	0.74–1.05	0.91	4.12 ± 0.43	1.54 ± 0.16	1.54 ± 0.10
Blue	$<$-9.30	-9.54	1651	8.2 ± 0.4	5.0	0.74–1.05	0.91	4.70 ± 0.35	1.62 ± 0.13	1.67 ± 0.09
Blue[b]	-8.60 − -8.95	-8.79	2451	3.9 ± 0.2	2.9	0.74–1.40	1.12	3.29 ± 0.35	1.30 ± 0.28	1.59 ± 0.15
Blue	-8.95 − -9.30	-9.11	2681	5.2 ± 0.2	1.4	0.74–1.40	1.07	4.13 ± 0.21	1.66 ± 0.16	1.64 ± 0.07
Blue	$<$-9.30	-9.54	2013	3.9 ± 0.2	1.6	0.74–1.40	1.03	4.64 ± 0.26	1.83 ± 0.17	1.76 ± 0.08
Red[a]	-9.90 − -10.6	-10.28	847	4.2 ± 0.3	2.0	0.74–1.05	0.90	4.82 ± 0.35	1.43 ± 0.32	1.86 ± 0.13
Red	$<$-10.6	-10.91	795	4.0 ± 0.3	2.7	0.74–1.05	0.89	5.04 ± 0.32	2.04 ± 0.25	1.81 ± 0.11

[a] $z<$1.05 galaxy samples are limited to $M_B<$-20.5.
[b] $z<$1.4 galaxy samples are limited to $M_B<$-21.0 .